DELFT UNIVERSITY OF TECHNOLOGY
FACULTY OF CIVIL ENGINEERING AND GEOSCIENCES

Climate & Weather and Earth Observation

Towards Delineating Channel Meltwater Extent Using Sentinel-1 on Greenland: An Assessment of Challenges and Limitations

---

Presented by
N.E.J. (Niels) van Boldrik

Defence to be held by June 11th, with examination committee consisting of:

Dr. Ir. B. (Bert) Wouters	**Primary Supervisor**
Dr. S.L.M. (Stef) Lhermitte	**Secondary Supervisor**

Academic year 2023-2024

Abstract

Global warming is accelerating the melting of glaciers and ice sheets, leading to the formation of supraglacial meltwater, which accumulates in supraglacial lakes and significantly impacts glacier stability. Supraglacial channels can redistribute meltwater and improve glacier stability and are currently monitored using optical data from Sentinel-2. Using Sentinel-1 synthetic aperture radar data omits issues related to cloud cover and darkness, which is the primary focus of this study. The study focuses on three glacier site subsections: Nioghalvfjerdsbrae Glacier, Humboldt Glacier, and Russell Glacier. Sentinel-1 data is compared to the well-established optical data from Sentinel-2, which serves as the reference for channel delineation.

The methodology encompasses both thresholding techniques and a GLCM-assisted random forest regression for co- and cross-polarized Sentinel-1 data, while Sentinel-2 data utilizes a thresholding technique based on Glen et al. (2024) and a path-opening algorithm developed by Yang et al. (2015) to delineate narrow channels from enhanced NDWI images. Google Earth Engine is employed for data access and preprocessing, whereas Python is leveraged to conduct the subsequent analysis.

Preliminary studies have shown that individual Sentinel-1 scenes may only partially capture supraglacial channels. Therefore, individual scenes are aggregated by taking the backscatter minimum (assumed to be indicative of water due to specular reflection) and standard deviation (representative of change) over a melt season. Composite images offer a more comprehensive view of the supraglacial drainage network during the melt season and form the basis for GLCM texture feature calculations. A 3-by-3 kernel is used around pixels to generate an additional 64 input features by calculating the contrast, correlation, heterogeneity, and dissimilarity over 4 discrete angles for the HH and HV minima and variance. The backscatter features are fed through a random forest regressor with the per-pixel water fraction (i.e. the fraction of which each pixel is classified as water over all images) as the target variable derived from the Sentinel-2 reference classification, providing a more flexible regressor than a binary distinction.

Results indicate that channels with sufficient cross-sectional area are detectable in Sentinel-1 data for both polarizations, albeit with varying success. Challenges such as speckle noise, channel size, the heterogeneity of pixel elements, and the movement of glaciers complicate the analysis. The study finds that while thresholding outperforms GLCM-assisted regression, both methods struggle with speckle noise inherent in Sentinel-1 data and alignment issues between the model input and reference classification. Despite these challenges, GLCM-assisted regression shows promising results by leveraging textural information and outweighing backscatter minima and variances in terms of feature importance.

To conclude, Sentinel-1 data can be incorporated to delineate channels of sufficient size. Channels approaching the pixel resolution are captured partially at best and require image compositing. The variability in terrain and channel features, alongside persistent noise, limits the accuracy and reliability of this approach. GLCM texture feature analysis and random forest regression show promising results despite the multitude of problems. Other machine-learning techniques should be explored prior to continuing with this approach.

Contents

1. Introduction

Global warming has become a pressing concern, profoundly impacting various components of the cryosphere (IPCC, 2021). One of the most significant consequences of rising temperatures is the increased melting of glaciers and ice sheets. This process leads to the formation of meltwater, which plays a crucial role in the dynamics of ice masses. Meltwater generated on the surface of glaciers, known as supraglacial meltwater, can significantly influence glacier behaviour and stability. The increasing amounts of meltwater volume require more accommodation space to be stored and is generally done in supraglacial lakes, which may be interconnected by supraglacial channels. Excessive amounts of meltwater accumulation apply significant pressure on the ice surface, possibly resulting in hydrofracturing. Hydrofracturing occurs when water percolates through crevasses and fractures, reaching the glacier bed. Water seeps down through cracks and lubricates the ice-bed interface. Lubrication reduces basal friction and allows the ice to move more easily, potentially causing a sudden increase in glacier flow rates and contributing to the (temporary) destabilization of the ice sheet (Rignot et al., 2004; Scambos et al., 2000). To mitigate the accumulation of meltwater and, in turn, aid in ice sheet stability, supraglacial channels serve as natural conduits and redistribute meltwater to areas where it may be stored and drained more effectively (Bell et al., 2017). Accurate mapping of these features enables scientists to monitor changes in meltwater distribution and volume, which are critical for predicting the response of glaciers to warming temperatures.

Currently, supraglacial meltwater features are commonly mapped using optical imagery from the Landsat-8 and Sentinel-2 missions, as well as Synthetic Aperture Radar (SAR) data from Sentinel-1 (Jiang et al., 2022; Moussavi et al., 2020; Yang et al., 2019). However, optical systems rely on visible and infrared wavelengths, making them susceptible to cloud cover interference. Clouds obstruct the satellites' view of the Earth's surface, resulting in gaps or reduced quality in the collected data. If an image where most of the area is covered by opaque clouds, the surface underneath cannot be observed. On the other hand, transparent clouds can interfere with the signal and reduce image quality, as if you were to look through foggy glasses. This limitation poses challenges for continuous and accurate monitoring, as frequent cloud cover can hinder the constant acquisition of clear images. Furthermore, darkness prohibits optical instruments from capturing images completely. During winter, when polar night becomes more pronounced, fewer and fewer images meet interpretability standards (i.e. enough reflection of light). Fortunately, Sentinel-1 does not rely on illuminated surfaces and can penetrate through clouds. Contrary to the inconsistent acquisition time of Landsat-8 and Sentinel-2, Sentinel-1 supplies images with a static repeat cycle of 6 days. The ability to use Sentinel-1 data brings ample opportunity to improve the tracking of seasonal development of the supraglacial drainage network and assist where clouds hinder optical data. Nevertheless, SAR data is far more complex to interpret than its optical counterpart— rather than measuring reflectance in the visual spectrum (and infrared), analogous to our eyes, it measures reflectance in the microwave spectrum, referred to as backscatter.

Backscatter resembles the amount of energy scattered back towards the active sensor aboard the Sentinel-1 constellation. Unlike optical data, which is influenced primarily by surface colour and texture, SAR data is heavily dependent on the physical properties and conditions of the observed surfaces due to its longer wavelength. Various factors, such as surface roughness, moisture, and the dielectric properties of the target, influence backscatter. In the context of monitoring supraglacial meltwater features, the ability to distinguish the surrounding ice and (wet) snow from channels and lakes is pivotal. Due to the complex scattering mechanisms of (partially molten) snow and ice, this task is far from trivial. For example, liquid water content tends to smooth the surface, resulting in less surface roughness and decreasing the backscatter (Lund et al., 2022). On the contrary, liquid water content can increase volume scattering as a result of structural changes, which increases the backscatter (Ma et al., 2020). Due to this mixed interaction, melt may result in both less and more backscatter, highly dependent on the situation. Additionally, SAR data is contaminated with speckle noise, a granular interference arising from the coherent nature of radar waves. Essentially, propagating waves may amplify or extinguish one another due to resonance. Speckle is inherently different as it is multiplicative with the signal, whereas optical data mainly suffers from additive noise. This requires appropriate filtering techniques to reduce, typically involving some form of spatial averaging. For SAR, a stand-off is established between unfiltered-but-noisy and spatially-smoothed data, each presenting its advantages and disadvantages. Filtered data partially sacrifices small-scale detail but increases the overall image quality, whereas raw data preserves small-scale detail at the cost of higher noise levels.

This study aims to utilize Sentinel-1 data to delineate supraglacial channels in Greenland. So far, Sentinel-1 has mainly been used in river and floodwater mapping in a terrestrial setting and for supraglacial lake extraction on Greenland and Antarctica (Dirscherl et al., 2020; Jiang et al., 2022; Obida et al., 2019; Uddin et al., 2019), but it has yet to be applied for supraglacial channels. More commonly, Sentinel-2 is used for meltwater delineation and stands central in various thresholding methods, enhancement techniques and machine learning on both Greenland and Antarctica (Corr et al., 2022; Dirscherl et al., 2020; Lutz et al., 2023; Rawlins et al., 2023; Yang & Smith, 2012). This study utilizes a thresholding method by Glen et al. (2024) and an enhancement-based path-opening algorithm developed by Yang et al. (2015) to establish a Sentinel-2 meltwater delineation, which serves as a reference for Sentinel-1. The feasibility of Sentinel-1 data is assessed by examination of three study cases: the Humboldt Glacier in North-West Greenland studied by Rawlins et al. (2023); the Russell Glacier in South-West Greenland examined by Glen et al. (2024); and the Nioghalvfjerdsbrae (79°N) Glacier in North-East Greenland. Their respective time frames are the summer seasons of 2020, 2019 and 2020, matching those of their corresponding papers with the exception of the 79°N Glacier. Small subsections are used to examine what value Sentinel-1's consistent flux of SAR data holds compared to its optical successor in the context of channel meltwater delineation. Simple thresholding and a random forest regressor assisted by Gray-Level Co-occurrence Matrices (GLCMs) texture features are used experimentally in an attempt to delineate supraglacial meltwater features based on the Sentinel-2 reference.

By examining the three study cases, we aim to answer the following research questions:

- To what extent can Sentinel-1 data be used to identify supraglacial channels?
- What are the challenges of using Sentinel-1 for supraglacial channel delineation?
- What value do thresholding and GLCM-assisted random forest regression add in this context?

It is important to note that this topic is novel, and as such, this study is primarily exploratory. Chapter 2 introduces Google Earth Engine, the data utilized, corresponding preprocessing steps and study cases. Subsequently, Chapter 3 comprises the methods behind the meltwater delineation in supraglacial channels for both optical and SAR data. Regarding optical data, it explains Yang's path-opening algorithm and provides a Sentinel-2 classification scheme based on thresholding. For SAR, it addresses a thresholding technique and elaborates on GLCMs and their properties, which form the basis of the random forest machine learning inputs. Furthermore, it explains and motivates the use of composite images in addition to individual images. The results are given and discussed briefly in Chapter 4, followed by a more elaborate discussion in Chapter 5. Concluding remarks are presented in Chapter 6, after which some final recommendations are given in Chapter 7. Throughout most Figures, colour bars have been left out as the background-channel contrast is paramount rather than the absolute backscatter values.

2. Data and Study Areas

This chapter lists the data sources and platforms used throughout this study, along with three different study cases. Section 2.1 briefly considers Google Earth Engine, while Sections 2.2 and 2.3 elaborate on the satellite data and preprocessing. The three study cases are introduced in Section 2.4, after which their respective elevation models and ice velocities are given in Sections 2.5 and 2.6.

2.1 Google Earth Engine

Google Earth Engine (GEE) is an open, cloud-based platform that allows users to analyze and visualize geospatial data from various sources. It provides petabytes of satellite imagery and other geospatial datasets and enables users to analyze data without requiring extensive computational resources. GEE facilitates multiple applications such as environmental monitoring, land cover classification, and climate change analysis. This study uses it to access Sentinel-2 and Sentinel-1 data, as well as the Digital Elevation Model (DEM).

2.2 Sentinel-2 Data and Preprocessing

Sentinel-2 data provides a foundation for the supraglacial meltwater classification at a ground-level resolution of 10 metres for most bands. Whereas Sentinel-1 remains relatively unaffected by clouds, Sentinel-2 does not. Level-1C images with a cloud cover exceeding 50% are discarded, as well as those with a sun incidence angle less than 20° following Halberstadt et al. (2020). Low sun incidence angles can cause shadows to appear elongated, distorting the appearance of objects on the ground and affecting the accuracy of measurements (Halberstadt et al., 2020). Additionally, it can increase atmospheric scattering, resulting in degraded image quality and reduced contrast (Halberstadt et al., 2020). Rocks and clouds are masked following Corr et al. (2022) to differentiate snow, ice and water-covered surfaces from rocky surfaces and remaining cloud-covered areas using the Normalized Difference Snow Index (NDSI) and bands 2, 10 and 11, respectively. This masking utilizes the different spectral reflectance of these facies to identify and remove unwanted surface areas to avoid incorrect classification. Bands 10 and 11 are resampled bilinearly to ensure they match the 10-metre spatial resolution of band 2 to perform rock and cloud masking. Figure 3.1 in Section 3.1 provides a schematic including the preprocessing steps and extends this to a reference classification.

2.3 Sentinel-1 Data and Preprocessing

In an attempt to capture small-scale details like supraglacial channels, the Interferometric Wide swath (IW) acquisition mode of Sentinel-1 is utilized. The corresponding Level-1 Single Look Complex (SLC) spatial resolution of 5 by 20 metres translates to a 10-by-10 metre Level-1 Ground Range Detected (GRD) resolution, providing the highest publicly available ground resolution over Greenland. In addition to the co-polarized HH data, cross-polarized HV data is also extracted. The data is accessed through Google Earth Engine, in which each scene is preprocessed using the Sentinel-1 Toolbox (S1TBX), including thermal noise removal, radiometric calibration and terrain correction using the ASTER DEM. Each scene is manually subjected to an additional preprocessing step to correct for possible geometric distortions, establishing a proper spatial relationship of pixels implemented by Andreas Vollrath (ESA). Note that speckle reduction filters (e.g. refined Lee) are omitted to avoid any form of spatial averaging, as features of interest may be as small as the pixel size. Furthermore, the winter mean can be subtracted from each scene, potentially enhancing the contrast between surface melt and non-melt over summer. It is worth noting that this assumption inherits challenges regarding supraglacial lakes indicated by Zheng et al. (2023), as buried lakes may persist during winter and preserve their backscatter signature due to volume scattering, particularly for HV-polarization. However, as supraglacial lake delineation using Sentinel-1 has been studied by Zheng and others, we restrict ourselves to supraglacial channels (Dirscherl et al., 2021; Jiang et al., 2022; Miles et al., 2017).

2.4 Study Areas

The study areas are scattered across Greenland, each with unique meltwater features. Section 2.4.1 describes an area comprised of a broad and narrow river accompanied by meltwater ponds. These ponds are absent in the areas of Sections 2.4.2 and 2.4.3, the latter of which is characterized by (partial) surface melt. Furthermore, both areas contain supraglacial channels which may split or converge.

2.4.1 Nioghalvfjerdsbrae Glacier, North-East Greenland

The Nioghalvfjerdsbrae Glacier, also known as the 79°N Glacier, is located in North-East Greenland. The 79°N Glacier, much like the neighbouring Zachariae Isstrom Glacier, faces glacier retreat and is losing mass (Rignot et al., 2001; Sundal et al., 2009). Figure 2.1 highlights the study area within this glacier. The Nioghalvfjerdsfjorden form a 20-kilometre-wide catchment, considered a small region encompassing various supraglacial meltwater features. A large channel segment is present, accompanied by a narrower channel surrounded by meltwater ponds. Without motivation other than it being recent and an adequate example, satellite images from June 1st until September 1st, 2020, are used for this region, totalling 88 Sentinel-2 images and 30 Sentinel-1 images.

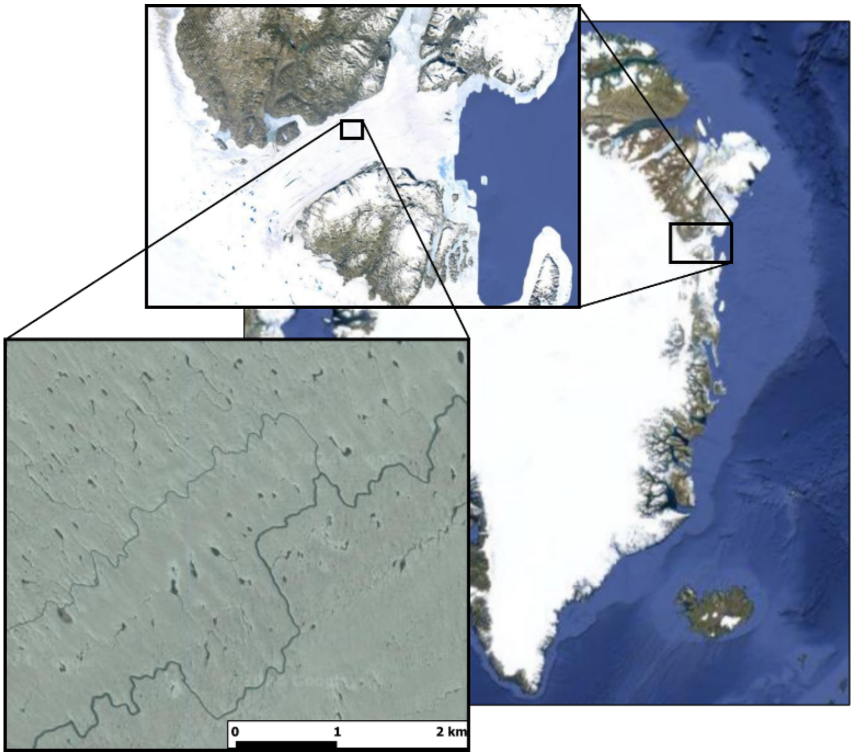

Figure 2.1: Patch on the Nioghalvfjerdsbrae (79°N) Glacier, North-East Greenland (image from Sentinel-2, 11-06-2020).

2.4.2 Humboldt Glacier, North-West Greenland

The Humboldt Glacier is located in North West Greenland and, similar to the Nioghalvfjerdsbrae Glacier, is also suffering from glacier retreat (Rignot et al., 2021). The glacier is projected to contribute significantly to the global sea level rise over the current century (Hillebrand et al., 2022). Its front is roughly 100 kilometres wide and discharges into the Kane basin shown in Figure 2.2 (first zoom-in).

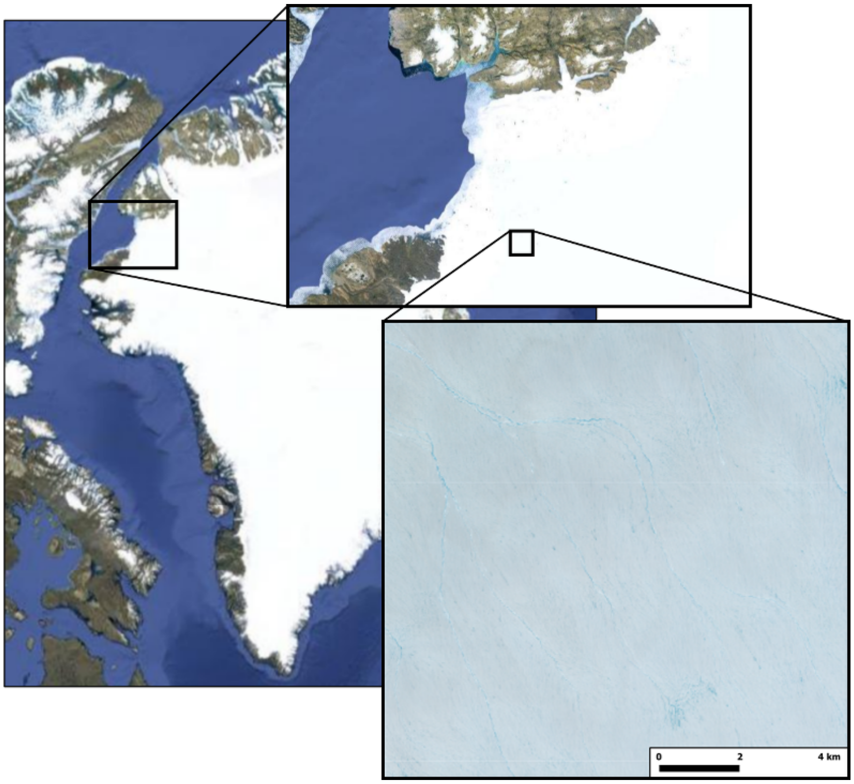

Figure 2.2: Patch on the Humboldt Glacier, North-West Greenland (image from Sentinel-2, 07-07-2020).

A channel-dominated area has been selected to study the capabilities of Sentinel-1 when it comes to capturing small-scale features. In a recent study, Rawlins et al. (2023) provided meltwater estimates for this area using Sentinel-2 data of 2020 but did not incorporate Sentinel-1 (Rawlins et al., 2023). Satellite images from June 1st until September 1st, 2020, are used for this region, totalling 111 Sentinel-2 images and 31 Sentinel-1 images.

2.4.3 Russell Glacier, South-West Greenland

The Russell Glacier is located in southwest Greenland and has recently been studied by Glen et al. (2024). The glacier flows westward from the Greenland Ice Sheet (GrIS) and possesses meltwater features such as channels, lakes and moulins. Figure 2.3 highlights the study area within the Russell Glacier.

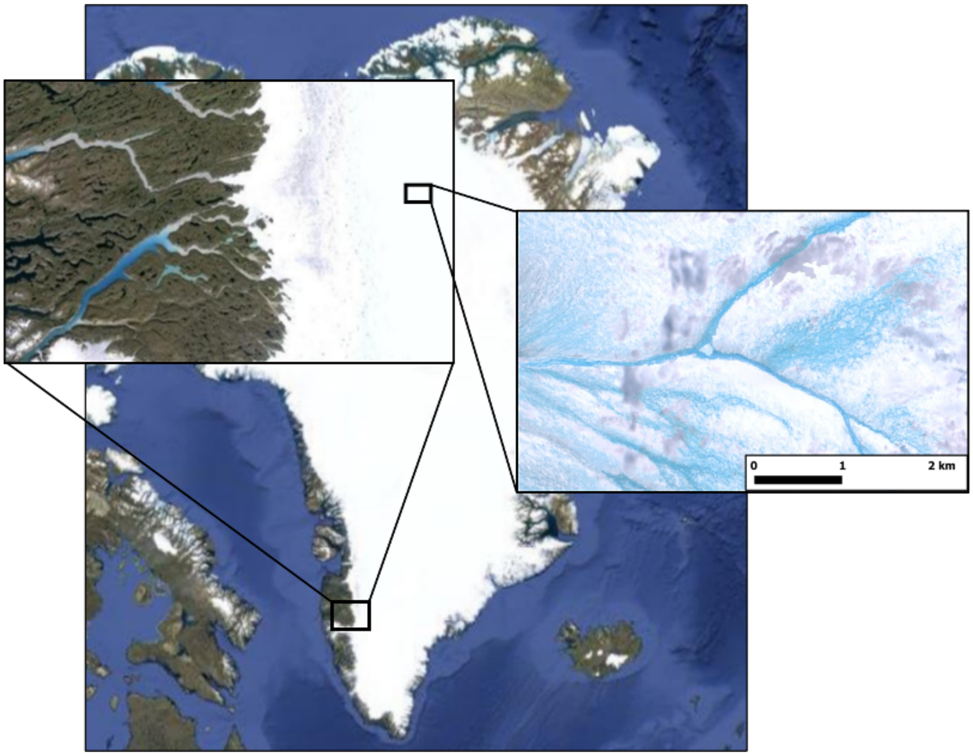

Figure 2.3: Patch on the Russell Glacier, Southwest Greenland (image from Sentinel-2, 12-07-2019).

A channel directed from East to West is present, along with melted or partially melted snow outside the channel, referred to as slush. Satellite images from June 1st until September 1st of 2019 are used for this region, comprising 30 Sentinel-2 images and 31 Sentinel-1 images for 2019. Meltwater features are prevalent throughout an exceptionally warm 2019, exposed to a mean summer temperature anomaly of 1.5°C compared to 2002-2016 (Sasgen et al., 2020). Regarding the Sentinel-1 data of this region, both images with and without subtraction of the winter mean are considered.

2.5 Digital Elevation Model

For the DEM, the ArcticDEM 2-metre mosaic is used (Polar Geospatial Center, 2024). The National Geospatial-Intelligence Agency (NGA) and the National Science Foundation (NSF) collaborated to form a high-resolution DEM over Greenland. Absolute accuracy has been improved by using IceSAT altimetry data on top of the optical stereo imagery. The DEM is given in Figure 2.4 for the three study cases.

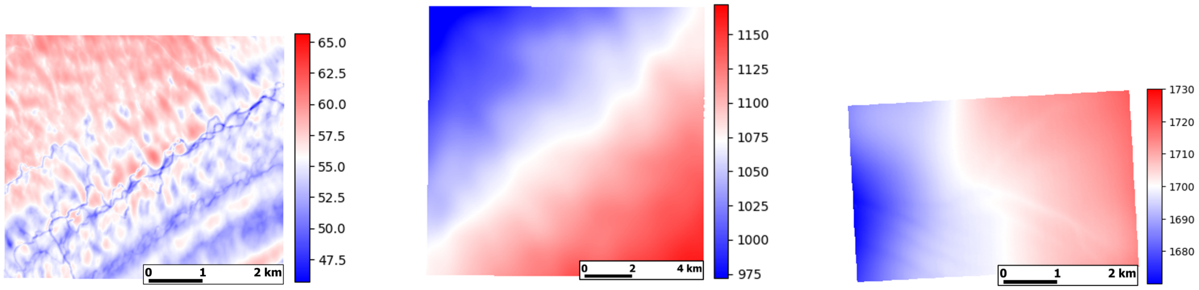

(a) 79°N Glacier. (b) Humboldt Glacier. (c) Russell Glacier.

Figure 2.4: Digital Elevation Models over the three study cases.

Note that the spatial and colour bar scales of the three study cases differ. The 79°N Glacier study case is relatively flat compared to the other two, resulting in visible small-scale detail mainly associated with the ponds and channels. The Humboldt and Russell study cases slope downward in a SE-NW and E-W direction, respectively. Their slopes lie between 0.5% and 1.0%, traversing roughly 50 to 100 metres for a vertical drop of 1 metre.

2.6 Ice Velocities

Figure 2.5 shows the ice velocities of the three study cases. Considering the three-month summer period from June to September and linking it to the pixel resolution of Sentinel-1 and Sentinel-2, the 79°N Glacier is expected to move roughly 270 metres (or 27 pixels). The Humboldt and Russell study cases move considerably less, totalling approximately 9 metres (1 pixel) and 45 metres (5 pixels), respectively. Movement is particularly important for compositing images without proper georeferencing since significant ice flows will stretch meltwater features, as is first observed and discussed in Section 4.2.1. Since this impacts the effectiveness of the approach described in Chapter 3, it is essential to keep the magnitude of the ice velocities in mind when analyzing the study cases.

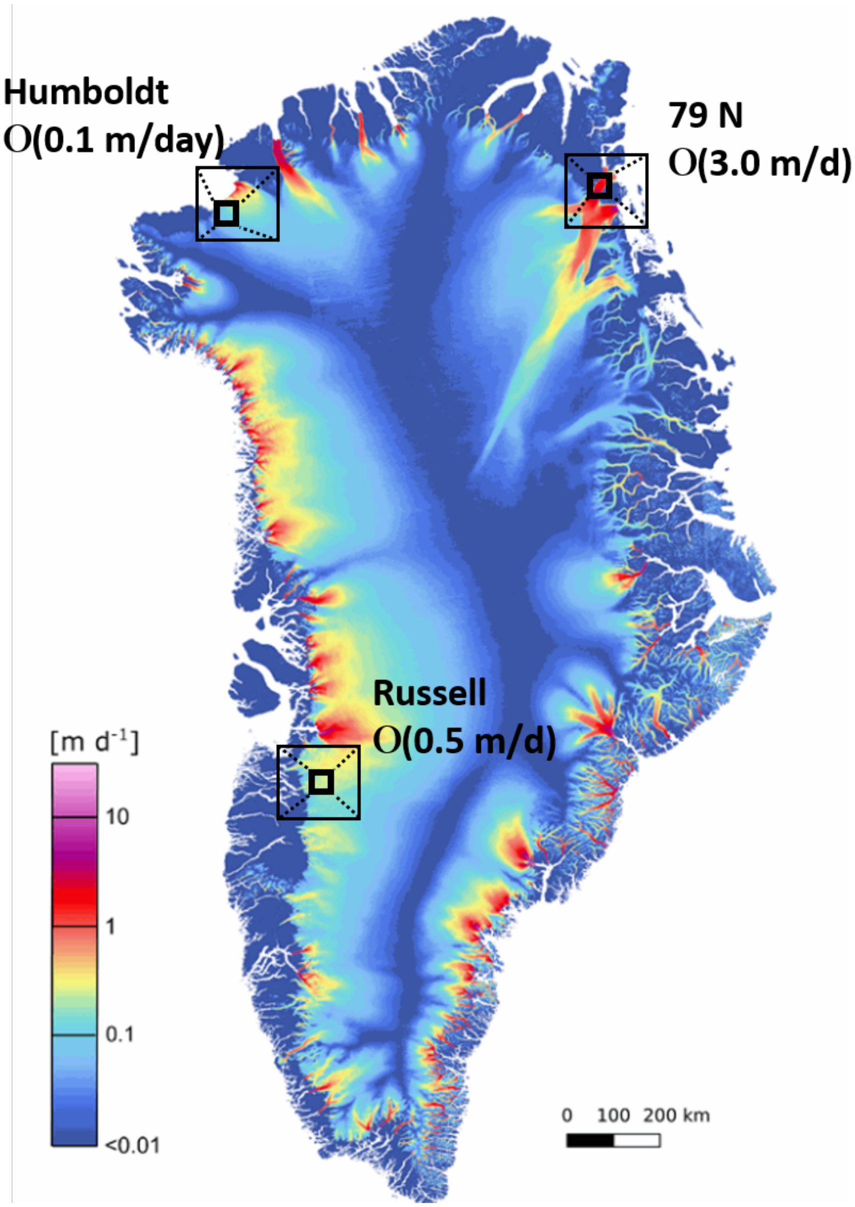

Figure 2.5: Approximate ice velocities of the three study cases averaged from October 2019 to October 2020 courtesy of the Copernicus programme (Copernicus, 2024).

3. Methodology

This chapter comprises the methodology behind meltwater delineation from Sentinel-2 and Sentinel-1 imagery. Section 3.1 explains how thresholding techniques are combined with the path-opening algorithm to attain a complete meltwater delineation from Sentinel-2 images, whereas Section 3.2 states how thresholding techniques and random forest are used similarly in an attempt to map meltwater channels from Sentinel-1 data.

3.1 Sentinel-2 Meltwater Delineation

Delineation from Sentinel-2 images comprises two methods applied case-dependently. Section 3.1.1 provides a meltwater delineation scheme applied to the Russell Glacier study case based on Glen et al. (2024). To delineate narrow channels, Section 3.1.2 briefly explains the key aspects of a morphological path-opening approach developed by Yang et al. (2015, 2016), which is used for the 79°N Glacier and Humboldt study cases. Section 3.1.3 describes how individual images are combined into a single channel delineation image and addresses the approaches for each study case.

3.1.1 Thresholding Approach

Using the preprocessed Sentinel-2 images, the approach Glen et al. (2024) take has been followed closely, resulting in a meltwater classification based on thresholding the Normalized Difference Water Index (NDWI), the NDWI compensated for ice (NDWI_{ice}), alongside combinations of bands 2, 3 and 4. Figure 3.1 summarises the classification approach based on Glen et al. (2024). Here, bands 10 and 11 are resampled to match the 10-metre resolution of other bands, after which the NDSI is computed and used to generate rock and cloud masks together with bands 2, 3, 10 and 11. Applying these masks on Sentinel-2 scenes in combination with thresholding the NDWI and NDWI_{ice} and combinations of bands 2, 3, and 4 ultimately results in a water classification. It is important to note that no manual enhancement is done, deviating from the original approach of Glen et al. (2024), potentially reducing the quality of the water classification.

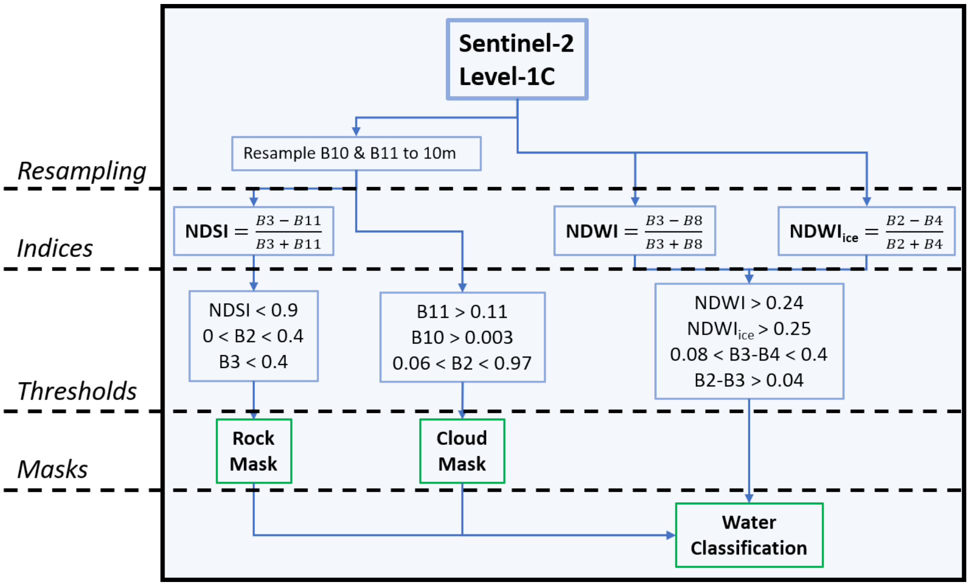

Figure 3.1: Adopted Sentinel-2 water classification scheme based on Glen et al. (2024)

3.1.2 Morphological Path-opening Approach

Various studies have successfully mapped supraglacial meltwater using NDWI and ice-adjusted NDWI thresholding techniques to delineate major channels and water bodies from surrounding elements (Hochreuther et al., 2021; Williamson et al., 2018). However, smaller channels may remain undetected due to their scale, resulting in insufficient reflectance for direct water classification. A morphological path-opening approach is used to delineate narrow channels (Rawlins et al., 2023; Yang et al., 2015, 2016, 2019) and can be summarised in 5 steps:

1. Initial channel delineation by applying an NDWI threshold.
2. Removing low-frequency image background and high-frequency image noise by using a *ramped bandpass filter*.
3. Convolving with a *multidirectional Gabor filter* to identify linear features (channels).
4. Applying a *path-opening operator* to connect channel segments resulting in enhanced images, encompassing a more complete delineation.
5. Combining the initial delineation and enhanced images.

A *ramped bandpass filter* is used to remove low-frequency image background and high-frequency image noise. Frequencies $f = [1/600, 1/200, 1/40, 1/20]$ m^{-1} are used given by Yang et al. (2016), preserving supraglacial channels, which enables their detection by applying the subsequent processing.[1] Its result is shown in the bottom left image of Figure 3.2 in which channels are retained.

---

[1] Filter frequencies slightly deviate from the frequencies used by Yang et al. (2016). However, they are the default settings of the corresponding Matlab code and have produced similar results.

The *Gabor filter* is a complex sinusoidal waveform modulated by a Gaussian envelope, making it sensitive to both frequency and the orientation of textures within an image. As such, multiple filters are used with different angles in an attempt to capture channels with dynamic orientations. It is given by

$$g(x, y) = \frac{1}{2\pi\sigma_x\sigma_y} \exp\left[-\frac{1}{2}\frac{x^2}{\sigma_x^2} + \frac{y^2}{\sigma_y^2}\right] \cos(2\pi f_0 x), \tag{3.1}$$

where σ_x^2 and σ_y^2 are the variances in their respective directions and f_0 referring to the base frequency of the sinusoidal waveform. Transforming equation 3.1 to depend on angle θ, the spatial coordinates x and y are projected to x' and y' with

$$\begin{cases} g^\theta(x', y') = g(x, y) \\ x' = x\cos\theta + y\sin\theta \\ y' = y\cos\theta - x\sin\theta, \end{cases} \tag{3.2}$$

in which $g^\theta(x', y')$ is the Gabor filter defined for angle θ. Essentially, multiple Gabor filters with different orientations θ are convolved with the input image $I(x, y)$ given by

$$r^\theta(x, y) = g^\theta(x, y) * I(x, y), \tag{3.3}$$

where $r^\theta(x, y)$ is the Gabor filter response. To combine the filter responses into a single outcome (representing the orientation the channel is best defined by), the maximum magnitude is taken from the different filters following

$$r(x, y) = \max\left(r^\theta(x, y), \quad \theta \in [0, \pi)\right). \tag{3.4}$$

Throughout this study, a width of $w = 2$ (pixels) is used to focus on channels with scales close to the pixel resolution. Following Yang et al. (2015), the variances and modulation frequency are then given by $\sigma_x = \sigma_y = w/2(\sqrt{2\ln 2})$ and $f_0 = 1/w$. Furthermore, the Gabor filter responses are calculated over angles $\theta \in [0, \pi)$ with an interval of $\pi/12$ (15°). Note that the symmetry makes angles $\theta \geq \pi$ (180°) obsolete as the gradients would have an equal magnitude as their mirrored counterpart.

The *morphological path-opening operator* opens and closes linear features to connect channel segments and enhance their connectivity. Discretizing path orientations in angles 0°, 45°, 90°and 135° to identify neighbouring water pixels in combination with a parsimonious path opening (PPO) length of 20 pixels following Yang et al., 2015 is used to construct enhanced images from equation 3.4. A brightness threshold, $t = \mu_t + \sigma_t$, is used to classify water from the enhanced images, where μ_t and σ_t represent the mean and standard deviation of the brightness. This threshold is determined experimentally after examination of the study cases, but based on the initial recommendations by Yang et al. (2015). To do this operationally, a similar threshold is advised of the form $t = \mu_t + b\sigma_t$, where b is a scalar (Yang & Smith, 2012; Yang et al., 2015).

Finally, the initial delineation is combined with the classification from the enhanced images to form a thorough channel delineation. Applying this path-opening algorithm to a Sentinel-2 image of the Humboldt Glacier study case results in Figure 3.2, in which it is combined with an initial NDWI threshold of 0.4 following Rawlins et al. (2023). The image at the top right shows that the path-opening algorithm has accentuated narrow channels, whereas thresholding techniques would fail and only capture segments of the smaller channels. Their small scale interferes with the spatial resolution at which reflectance is measured, i.e. features are not large enough to reflect enough to be visible.

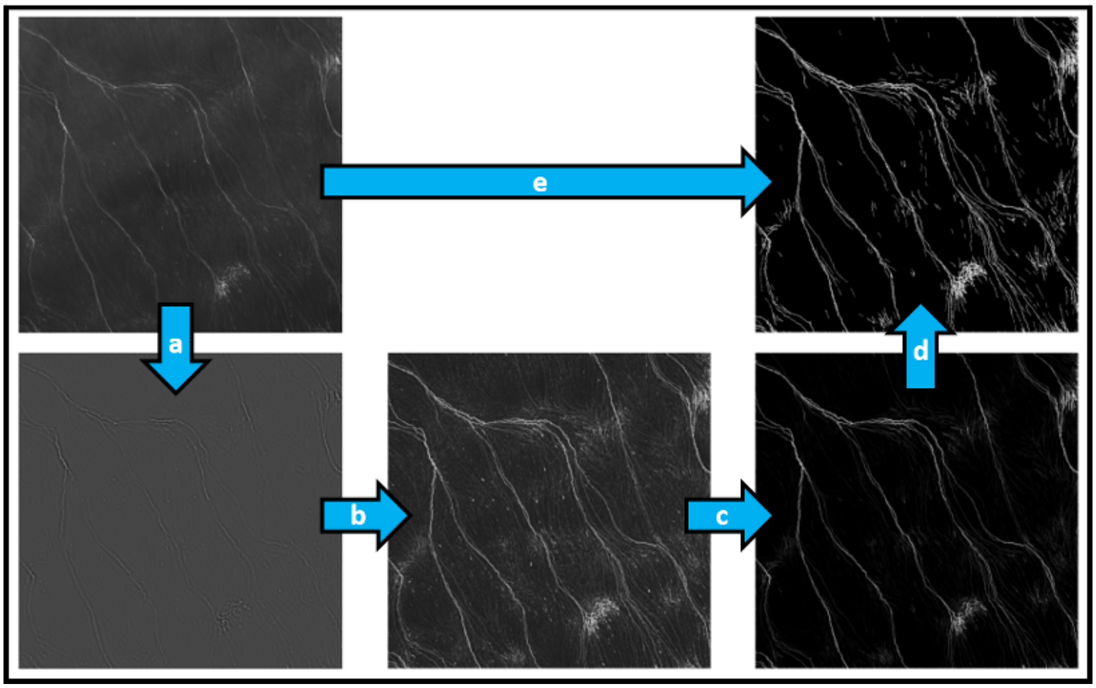

Figure 3.2: Reference Sentinel-2 water classification of a single NDWI image of the Humboldt study area. A ramped bandpass filter is applied (a) to the NDWI image, followed by a multidirectional Gabor filter (b) and the morphological path-opening operator (c). The initial NDWI threshold for water bodies and enhancement threshold combined provide the final classification (d, e).

3.1.3 Compositing Images

To 'stack' (also referred to as compositing) Sentinel-2 images, all images are classified and summed pixel-per-pixel to produce a single image. Pixel values range from 0 to 1 and represent the fraction f_w of images in which each pixel is classified as water, given by

$$f_w = \frac{n_{\text{water}}}{n_{\text{total}}}, \tag{3.5}$$

where n_{water} and n_{total} refer to the number of images in which that pixel is classified as water and the total number of images, respectively. Several thresholds of f_w are used to determine a final water classification depending on the study case. The thresholds for f_w are determined experimentally and could be optimized for each study case. However, since this research focuses on the applicability of Sentinel-1 and GLCM texture features rather than the quantification of meltwater, thresholds were based on visual inspection.

This study uses the thresholding technique in Figure 3.1 for the Russell catchment, following Glen et al. (2024). On the other hand, the region on the Humboldt glacier is subjected to an NDWI threshold of 0.4, and the path-opening algorithm for further delineation following Rawlins et al. (2023), which is also used for the 79°N Glacier study case.

3.2 Sentinel-1 Meltwater Delineation

Rather than stacking classification images as is done for Sentinel-2, Sentinel-1 images are stacked prior to the classification step described by Section 3.2.1. Section 3.2.2 briefly explains backscatter thresholding, whereas Section 3.2.3 elaborates on the random forest approach and purpose of GLCM texture features.

3.2.1 Compositing Images

Initial experimentation has shown that individual Sentinel-1 scenes do not gather the detail necessary to delineate the supraglacial channels to a similar extent to that of Sentinel-2 scenes (Section 4.2.2, Figure 4.13). As such, the focus shifted to mapping the overall supraglacial channel extent rather than that of individual images.

Sentinel-1 scenes are stacked differently compared to Sentinel-2—rather than classifying individual scenes and stacking them, the minimum backscatter values over the melt season are taken. Motivation is derived from the, perhaps naive, assumption that deep (and flat) enough surface water results in almost perfect specular reflection instead of diffuse reflection. The surface would act as a near-perfect mirror and reflect most of the incoming signal away from the sensor, resulting in extremely low backscatter intensities. In addition to the backscatter minima, the maxima have been examined during the preparation phase of this thesis and are speckly of nature without any form of structure.

The standard deviation over the melt season supports backscatter minima. With the occurrence of surface melt, surface characteristics change drastically. An increase in liquid water content, for example, increases the dielectric constant of the surface snow, which directly affects scattering properties. Furthermore, liquid water content tends to smooth the surface, resulting in less surface roughness and decreasing the backscatter (Lund et al., 2022). On the contrary, liquid water content increases volume scattering, which increases the backscatter (Ma et al., 2020). Changes in surface snow characteristics have complex interactions with various scattering mechanisms. They can both reduce and increase backscatter, which the standard deviation (or any metric of temporal variance) over the melt season should capture. As such, the backscatter minimum and standard deviation are taken as parameters on which to base the channel delineation.

3.2.2 Backscatter Thresholding

Two classification techniques are explored based on these parameters for both HH and HV-polarization data. Thresholding techniques (e.g. Otsu) have successfully delineated water from Sentinel-1 imagery in terrestrial context (Liang & Liu, 2020; Tan et al., 2023). This study takes this concept and attempts to apply it in a glacial context, thresholding individual and composite Sentinel-1 scenes to distinguish meltwater from neighbouring features whilst focusing on channels. For simplicity, static backscatter thresholds are applied to compare the results to those of the random forest regressor.

3.2.3 GLCM-assisted Random Forest Regression

To compare thresholding to an alternative approach, random forest regression is exploited.[2] The minima and standard deviations are accompanied by Gray Level Co-occurrence Matrices (GLCMs) inheriting texture features which may differ between surface elements. GLCMs have previously been used for vegetation mapping and sea ice classification using both Sentinel-1 and Sentinel-2 data (Caballero et al.,

---

[2] The random forest models used throughout this study utilize the default settings provided by `sklearn`. Hyperparameters have not been optimized following the results.

2020; Mohammadpour et al., 2022). In an attempt to extend this to channel delineation, they are included in the random forest regression. The GLCM texture features of consideration are

$$\begin{cases} \sum_{i,j=0}^{levels-1} P_{i,j}(i-j)^2 & \text{contrast} \\ \sum_{i,j=0}^{levels-1} P_{i,j}\left[\frac{(i-\mu_i)(j-\mu_j)}{\sqrt{\sigma_i^2\sigma_j^2}}\right] & \text{correlation} \\ \sum_{i,j=0}^{levels-1} P_{i,j}\frac{P_{i,j}}{1+(i-j)^2} & \text{homogeneity} \\ \sum_{i,j=0}^{levels-1} P_{i,j}|i-j| & \text{dissimilarity,} \end{cases} \tag{3.6}$$

where $P_{i,j}$ refers to the number of times that gray-level j occurs at a distance d and an angle θ from gray-level i. Gray levels range from 0 to 255 (8-bit) and resemble the gray-scaled pixel intensity. Texture features may differ for water patches compared to other patches, exemplified in Figure 3.3.[3]

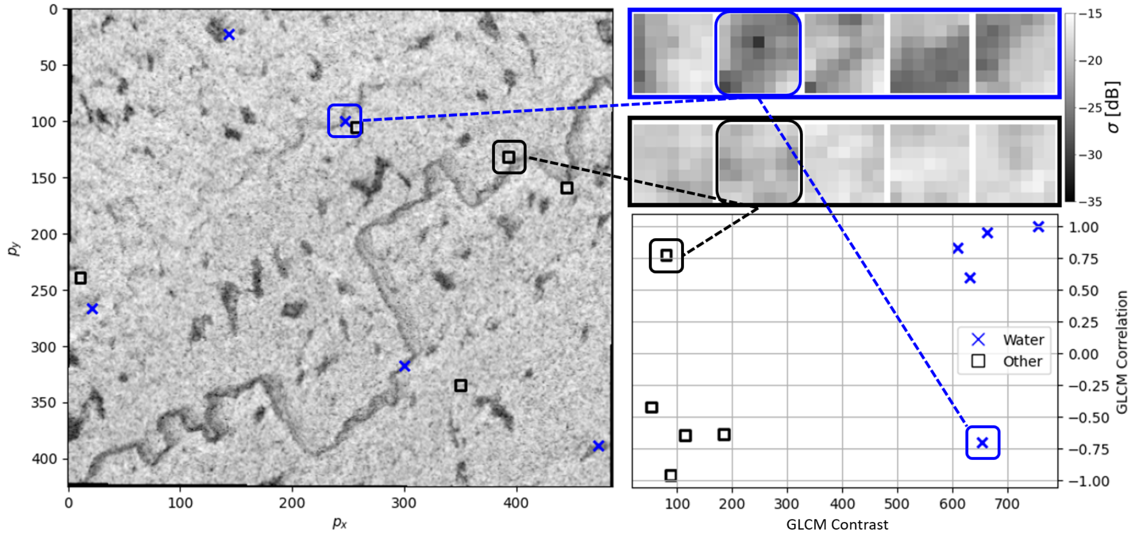

Figure 3.3: GLCM texture features for different surface patches. On the left side, the HH-polarized minimum backscatter of the 79°N Glacier study case is given (Section 4.1, Figure 4.6). The top right contains a 7-by-7 zoom-in of the water (blue) and other (black) patches. The bottom right highlights how the texture features (e.g. contrast and correlation) appear to be grouped together for different backgrounds. The GLCM texture features have been calculated over the inner 3-by-3 section. Two outliers have been indicated.

Due to the small-scale nature of supraglacial channels, a distance of 1 (pixel) is taken over a 3-by-3 kernel. Angles $\theta = [0°, 45°, 90°, 135°]$ are used to attain discretized multidirectional texture features accounting for complex channel geometries. Ultimately, this results in a 4-dimensional matrix $P[i, j, d, \theta]$. Texture features and the backscatter statistics are fed through a random forest regressor with the Sentinel-2-derived per-pixel water classification fraction as the target variable. Rather than restricting the regressor to a binary target, the water fraction is used to provide a more flexible target in the event of incorrect classifications. Additionally, the maximum NDWI is taken as the target experimentally for the Humboldt study case since the initial regression results (Section 4.2.3, Figure 4.18a) were insignificant. Motivation

---

[3] These patches have been cherry-picked for illustration purposes and are not representative of *all* patches.

is derived from the expectation of high values (approaching 1) for the NDWI in water pixels and lower (near 0) for non-water pixels. It is important to note that this is susceptible to noise and outliers.

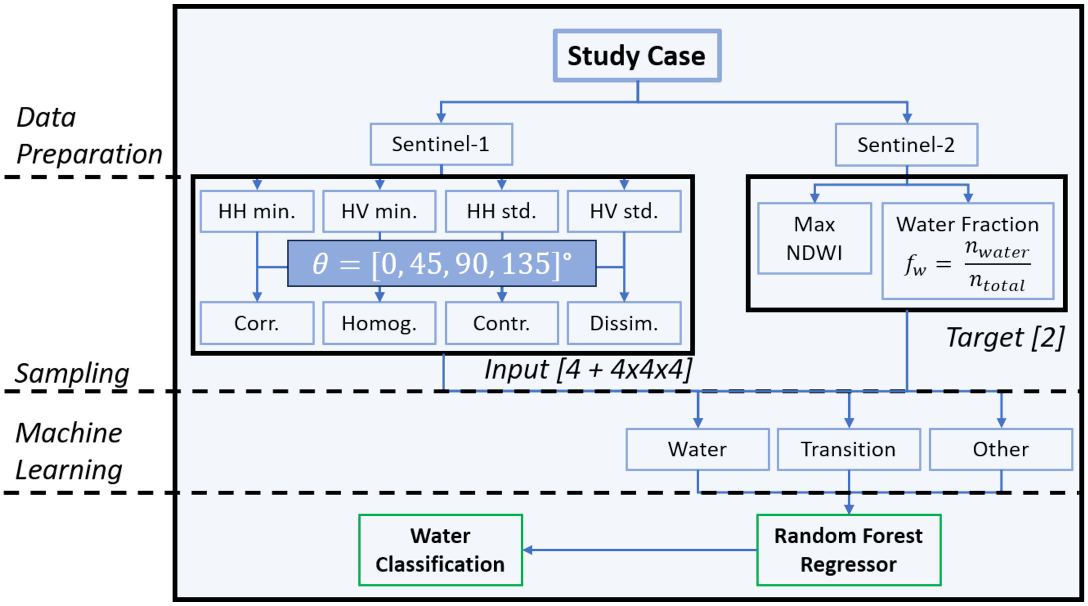

Figure 3.4: Machine learning approach employing GLCM calculations on backscatter properties to provide input data, whilst the NDWI and water fraction provide target data for the random forest regressor.

Figure 3.4 provides a schematic of the machine learning approach. Sentinel-1 offers 4 different images (HH and HV variances and minima), for each of which 4 GLCM properties are computed across 4 different angles, resulting in 4 base images with $4 \times 4 \times 4 = 64$ additional inputs for the random forest model (68 total). For sampling, 3 different 'classes' are considered—water pixels, 'other' pixels and so-called transition pixels, which are adjacent to water pixels. These transition pixels are included experimentally in the Humboldt study case due to the suspicion of minor misalignment, which would be problematic at pixel-level feature scales. Sampling is done randomly, stressing that the Sentinel-2-based classification should be correct at a pixel-level scale.

The regression value, referred to as p, resembles the water fraction, mimicking the 'probability' of a pixel being water. Note that this does not range from 0 to 1 but from 0 to the maximum fraction from the Sentinel-2 image. As such, it is not an actual probability. To translate this to a binary classification, both f_w and p are thresholded to distinguish water pixels from non-water pixels. Alternatively, f_w can be thresholded before training and used as a binary target variable, although this would likely reduce the flexibility of the regressor. To assess the quality of the random forest regression results, thresholds for f_w and p are taken to generate a binary classification. Next, the accuracy, precision, recall and F1 score are computed to quantify the results and possibly locate the source of errors, defined by

$$
\begin{cases}
\text{Accuracy} = \dfrac{\text{TP} + \text{TN}}{\text{Total Observations}} \\
\text{Precision} = \dfrac{\text{TP}}{\text{TP} + \text{FP}} \\
\text{Recall} = \dfrac{\text{TP}}{\text{TP} + \text{FN}} \\
\text{F1 Score} = 2 \times \dfrac{\text{Precision} \times \text{Recall}}{\text{Precision} + \text{Recall}},
\end{cases}
\tag{3.7}
$$

where TP, TN, FP and FN are the number of true positives, true negatives, false positives and false negatives. Accuracy quantifies the overall correctness of the model, while precision and recall measure how many positive predictions are correct and how many actual positives are captured, respectively. Precision is particularly sensitive to the number of false positives, whereas recall is susceptible to the number of false negatives. In the context of channel meltwater delineation from Sentinel-1 using Sentinel-2 as a reference, these measures are informative of incorrect classification of Sentinel-1, but also of water that Sentinel-2 may miss. Finally, the F1 score provides a balanced evaluation of precision and recall.

Two image sets (HH and HV minima and variances) containing the images before and after subtraction of the winter mean are utilized for GLCM calculations to analyze the effect of subtracting the winter mean. This is done in the Russell study case, as subtracting the winter mean severely degraded the image quality in the other two study cases. By examining the feature importance within the regressor, possible conclusions may be drawn with regard to the effect of subtracting the winter mean.

4. Results

This chapter contains the results of applying the methods to the study cases stated in the previous chapter. Sections 4.1, 4.2, and 4.3 govern the findings of the 79°N, Humboldt and Russell Glaciers.

4.1 Nioghalvfjerdsbrae Glacier

This section governs the results of the 79°N Glacier study case. First, Section 4.1.1 provides the reference data and delineation based on Sentinel-2, after which Section 4.1.2 relates this to the Sentinel-1 data. Section 4.1.3 employs the GLCM-based random forest approach on a small subsection, followed by a summary of findings in Section 4.1.4.

4.1.1 Sentinel-2 Data and Delineation

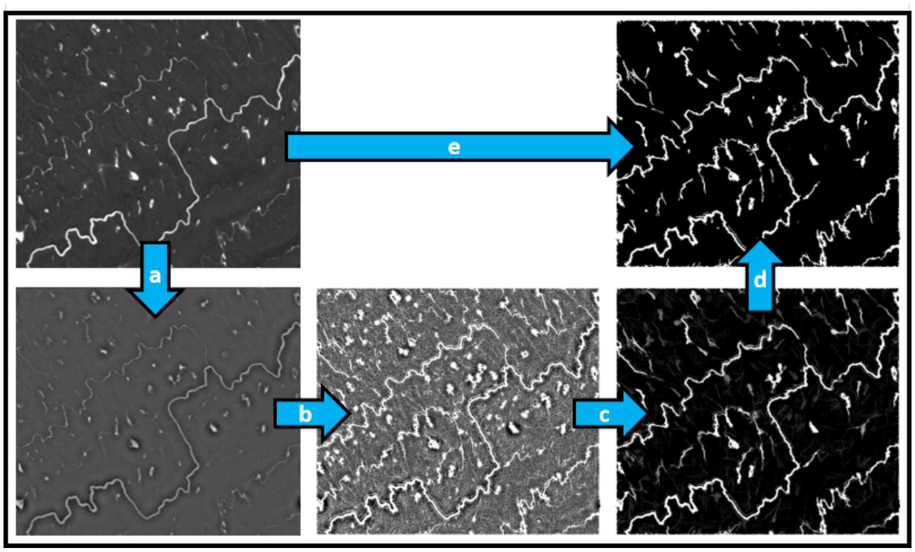

Figure 4.1: Sentinel-2 water classification of a single NDWI image of the 79°N Glacier study case. A ramped bandpass filter is applied (a) to the NDWI image, followed by a multidirectional Gabor filter (b) and the morphological path-opening operator (c). The initial NDWI threshold for water bodies and enhancement threshold combined provide the final classification (d, e).

For simplicity, the approach from Rawlins et al. (2023) is taken for the 79°N Glacier. Figure 4.1 shows typical delineation results following Section 3.1.2. One can see that the enhancement leads to an adequate identification of the narrow channel. The main channel and meltwater ponds are preserved, creating the complete Sentinel-2 water classification. However, some imperfections present themselves, as will be pointed out in Section 4.1.2. To supply Sentinel-2 reference scenes for the upcoming Sentinel-1 scenes, consider Figure 4.2.

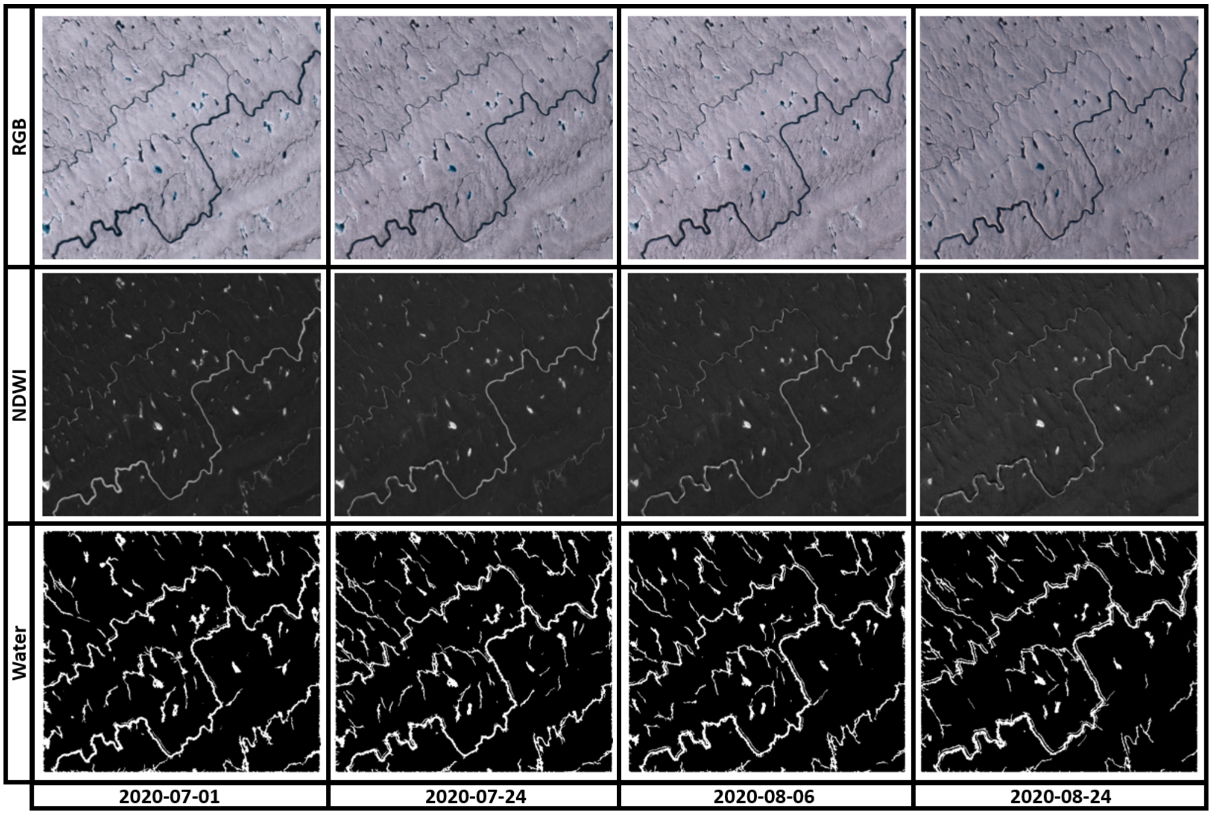

Figure 4.2: Subset of Sentinel-2 RGB (top), NDWI (middle) and water classification (bottom) images of the 79°N Glacier study case taken between July and September 2020.

Each of these individual scenes portrays the meltwater features and provides a reference for the individual Sentinel-1 scenes of similar date given in Section 4.1.2, Figure 4.4. The images are enhanced and stacked following Section 3.1, given in Figure 4.3. Taking the water classification fraction f_w in Figure 4.3a and applying a threshold results in Figures 4.3b and 4.3c, generating binary water classifications from the water fraction.

(a) Water fraction f_w [0-1]. (b) Classification ($f_w \geq 0.2$). (c) Classification ($f_w \geq 0.3$).

Figure 4.3: Sentinel-2 water classification of the 79°N Glacier study area from June to September 2020. Fraction f_w corresponds to the fraction of images in which a pixel is classified as water.

4.1.2 Sentinel-1 Data and Comparison

Figure 4.4 contains Sentinel-1 images taken at similar times to the Sentinel-2 images from Figure 4.2. The main channel is distinguished from the surroundings, and a simple brightness threshold suffices to delineate it. On the other hand, the narrower channel above is less visible. To confirm, Figure 4.5 compares the Sentinel-2 reference classification and a threshold-based Sentinel-1 classification of an individual image.

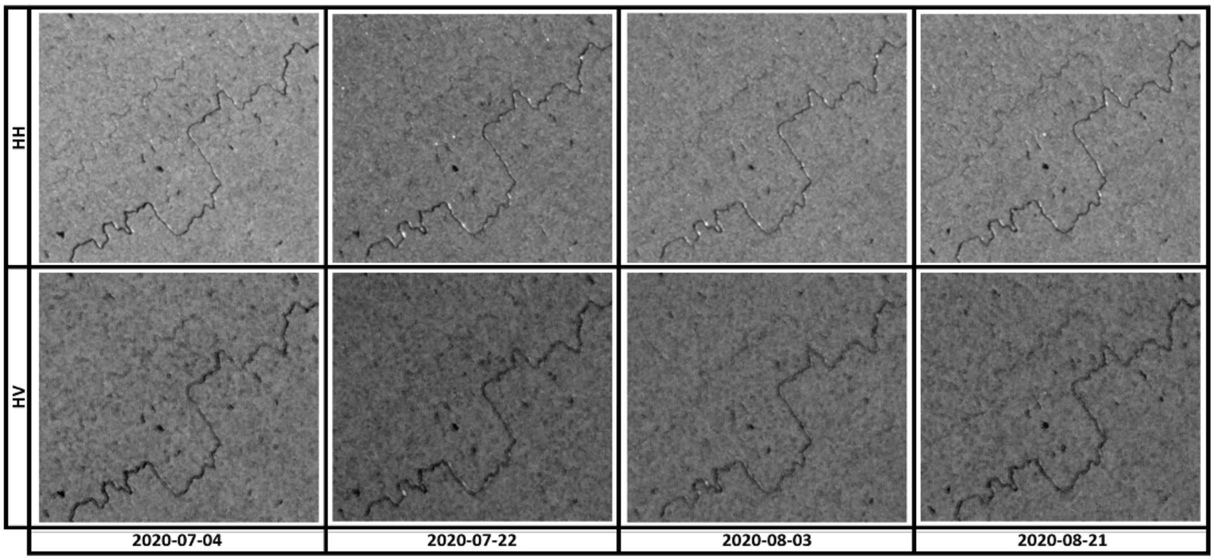

Figure 4.4: Subset of the Sentinel-1 HH-polarization (top) and HV-polarization (bottom) images of the 79°N Glacier study case taken between July and September 2020.

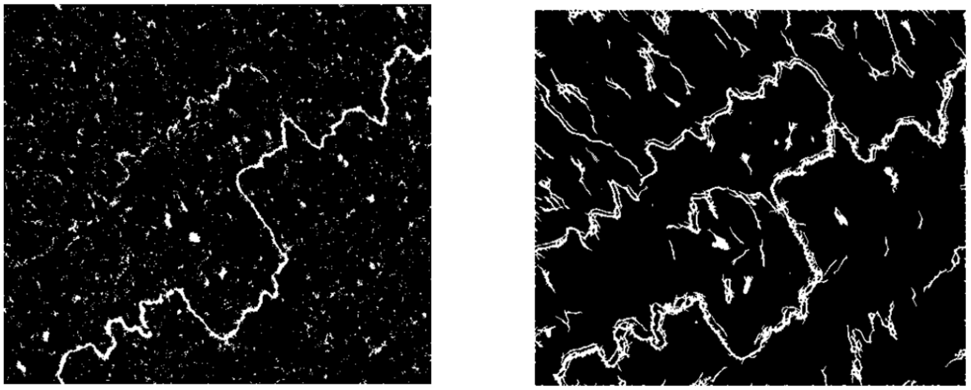

(a) Sentinel-1 thresholded ($t = -15$ dB) water classification of 2020-08-21.

(b) Sentinel-2 reference water classification of 2020-08-24.

Figure 4.5: Comparison of Sentinel-1 thresholded classification and reference Sentinel-2 classification of the 79°N Glacier study case.

Some noteworthy observations are that the Sentinel-1 classification (Figure 4.5a) captures the main channel (as well as the larger ponds). However, it fails to capture the secondary channel fully. Due to the inherited speckle noise, small granular patches are also classified as water. One can remove water patches (i.e. adjacent water pixels) of a given size to counteract this, although doing so is subject to the risk of eliminating actual water.

What is more striking are the artefacts in Figure 4.5b. As a result of the bandpass filter frequencies and channel width parameter w, the path-opening algorithm tends to 'duplicate' channel segments parallel to the channel orientation. This issue can be partially mitigated by experimentally adapting the bandpass frequencies depending on the image and area and adapting w to the target channel. Furthermore, the edges of the image are contaminated with a different type of artefact—pixels at the border are classified as water due to the 2-dimensional convolution part of the Gabor filtering step. Steep gradients appear and are carried over into the morphological path-opening step, resulting in the false identification of small channel segments.

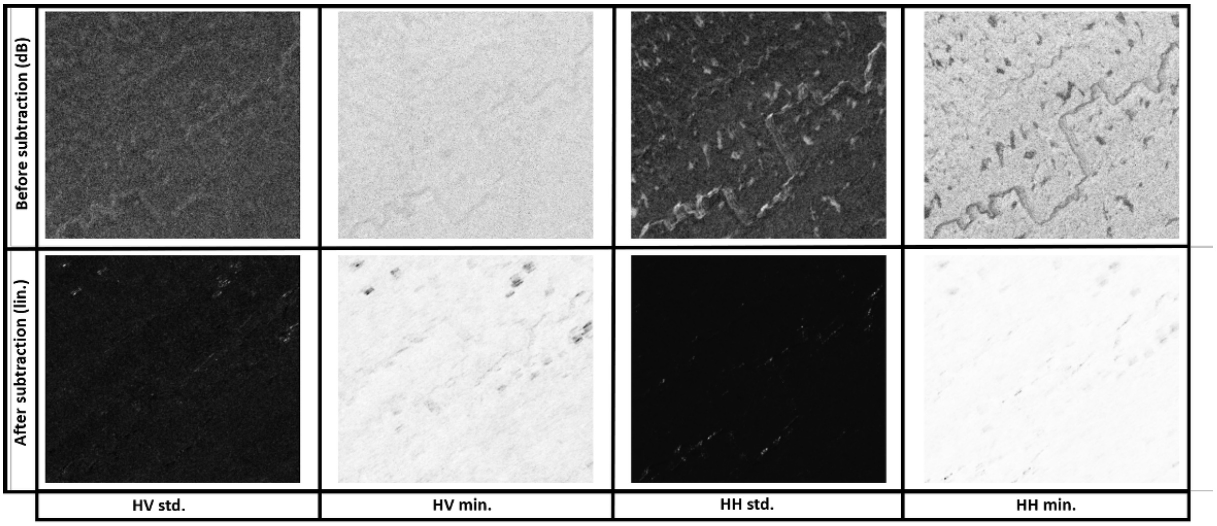

Figure 4.6: Co- and cross-polarized Sentinel-1 backscatter minima and standard deviations from June to September 2020 on the 79°N Glacier study area before (dB units) and after (linear units) subtraction of the winter mean.

Figure 4.6 shows that when compositing images, another issue arises. Considering multiple images of the same geometry are compressed into a single image, it is implied that the surface is static in time. This is not the case due to ice movement or glacier flow, highlighted in particular by the images before subtraction of the winter mean. The main channel appears to be elongated in an approximate SW-NE direction, coinciding with the movement direction of the ice sheet. Subtracting the winter mean is ineffective since, during winter, this geometry corresponds to a different surface, and the temporal mean itself is of a moving surface. Therefore, the subtraction of the winter mean is omitted.

4.1.3 Random Forest Regression

Figure 4.7 zooms in on a subsection of the area to examine using the random forest approach. To do this, 5000 water samples ($f_w \geq 0.25$) and 5000 other samples ($f_w < 0.25$) from the complete image are taken, each for which the GLCM parameters are calculated. The Sentinel-2 water fraction is used as the target parameter for the random forest model, of which the results are given in Figure 4.8. The regression values shown in Figure 4.8a are cubed to enhance the contrast in Figure 4.8b.

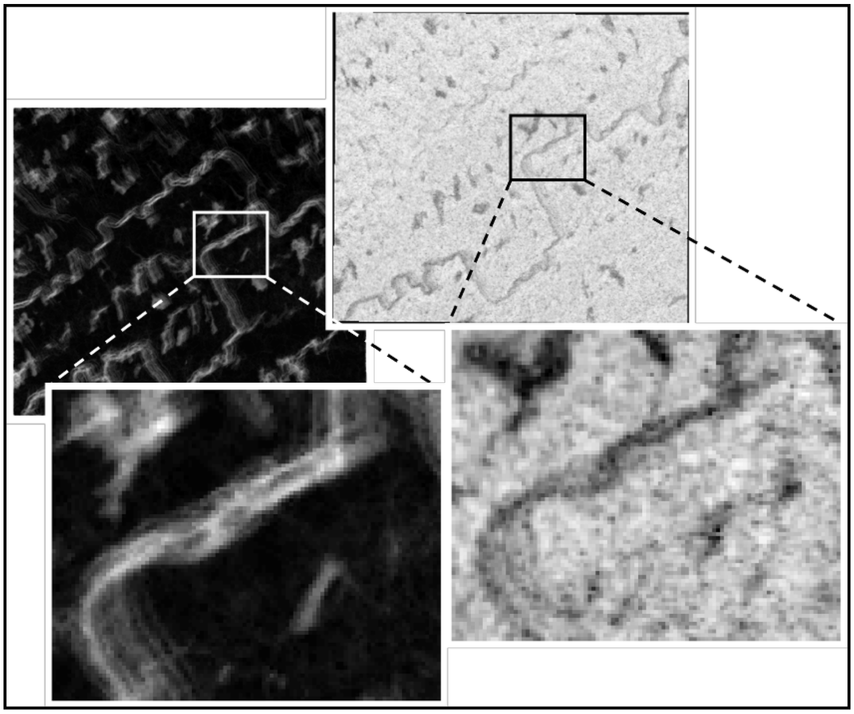

Figure 4.7: 79°N Glacier zoom in on Sentinel-2 classification and the HH minimum image of Sentinel-1.

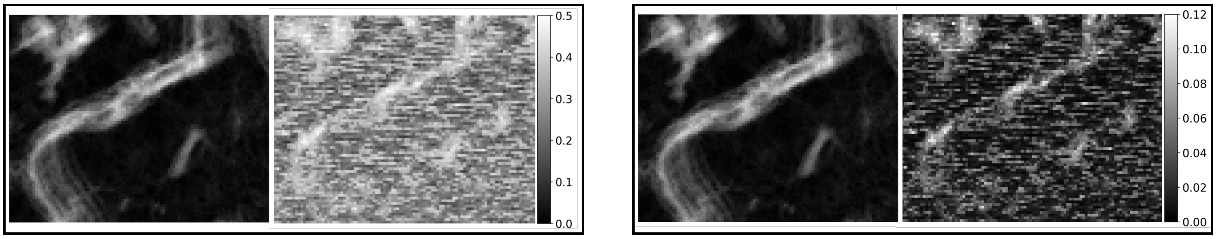

(a) Linear random forest model results (right) with water fraction (left) as the target variable.

(b) Cubed random forest model results (right) with water fraction (left) as the target variable.

Figure 4.8: Random forest model results for a small subsection when trained on 5000 water and other samples with GLCM properties on the 79°N Glacier study case. Brightness (unitless) on the images on the left corresponds to water fraction f_w and regression value p on the images on the right.

One can observe that the random forest approach with GLCM parameters can partially capture the channel. Additionally, the classification remains to suffer from a noisy background. Classification results are compared to the reference in Figure 4.9, of which the corresponding fractions and quality metrics are given in Table 4.1.

Classification	Fraction [-]
True Positives (TP)	0.114
True Negatives (TN)	0.623
False Positives (FP)	0.157
False Negatives (FN)	0.106

Metric	Score [-]
Accuracy	0.734
Precision	0.421
Recall	0.517
F1-score	0.464

Table 4.1: Random forest classification quality metrics and error fractions compared to the Sentinel-2 reference classification.

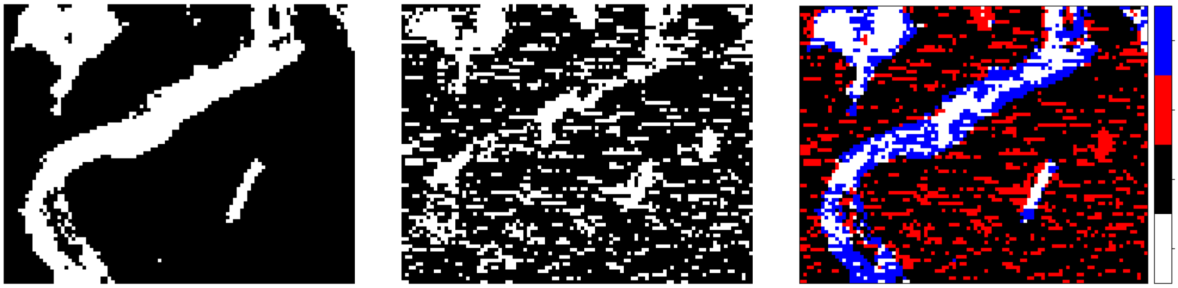

(a) Sentinel-2 Reference.

(b) Sentinel-1 Prediction.

(c) Random forest errors.

Figure 4.9: Random forest classification errors between binary Sentinel-1 and Sentinel-2 labels based on Figure 4.8. For Figures 4.9a and 4.9b, pixels with $f_w > 0.25$ and $p > 0.35$ are considered water, respectively.

Overall accuracy is at an acceptable 73.4%, though precision, recall, and F1-score indicate mediocre performance. The thresholds used for f_w and p are picked manually to visualize the spatial distribution of errors and could be optimized to increase the model performance.[1] False positives are primarily derived from the granular regression results scattered across the image. With a focus on the channel, there appears to be an approximately equal split of false negatives and true positives. A similar balance occurs between the speckly false positives and the true negatives for the non-water area.

Examining feature importance confirms that the HH minima is the most important factor by a significant margin. Table 4.2 gives the top 5 features, whereas table 4.3 summarises all features. The relevance of the GLCM features is rather limited—the HH minimum is significantly more important for the regressor than any of the other backscatter properties or GLCM features.

---

[1] Technically, these thresholds should be identical as p is the regressor value of f_w. However, decreasing p to match f_w vastly increases the FP proportion (red, Figure 4.9c) and results in worse performance metrics.

Feature	Importance
HH min.	0.34512
HH std. contrast 45°	0.07260
HH std.	0.04504
HV min.	0.01908
HH std. contrast 90°	0.01680

Table 4.2: Top 5 features based on feature importance of the 79°N Glacier study case.

Feature	Importance
HH min.	0.34512
HH std.	0.04504
HV min.	0.01908
HV std.	0.01485
Correlation	0.00897
Contrast	0.01236
Dissimilarity	0.00549
Homogeneity	0.00917

Table 4.3: Feature importance summary of the 79°N Glacier study case. GLCM properties are averaged across angles.

Comparing the random forest results to the performance of thresholding the HH minimum, which appears to capture the channel best in Figure 4.6, all quality metrics show that this outperforms the random forest approach. Table 4.4 and Figure 4.10 contain the same results but for a thresholded Sentinel-1 HH-minimum classification. Threshold t has been determined visually to show that, in this case, thresholding outperforms the GLCM approach substantially. Different areas require different thresholds.

Classification	Fraction [-]
True Positives (TP)	0.121
True Negatives (TN)	0.731
False Positives (FP)	0.049
False Negatives (FN)	0.099

Metric	Score [-]
Accuracy	0.851
Precision	0.709
Recall	0.546
F1-score	0.617

Table 4.4: HH-minimum thresholded classification quality metrics and error fractions compared to the Sentinel-2 reference classification.

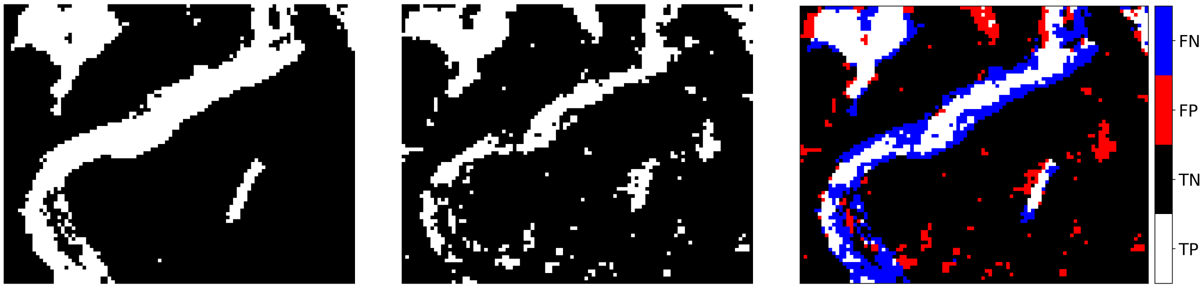

(a) Sentinel-2 Reference. (b) Sentinel-1 thresholded. (c) Random forest errors.

Figure 4.10: Random forest classification errors between binary Sentinel-1 and Sentinel-2 labels based on the HH-minimum in Figure 4.7. For Figures 4.10a and 4.10b, pixels with $f_w > 0.25$ and $t < -23$ dB are considered water.

4.1.4 Summary of Findings

Summarizing the findings of this study case is done with the following statements:

- Sentinel-1 adequately captures the main channel and most meltwater ponds in individual scenes for both polarizations (Figure 4.4).
- Speckle noise carries over to threshold-based classification. Removing small water patches may reduce this effect, but it comes with the risk of eliminating actual water bodies (Figure 4.5).
- Composite images for both Sentinel-1 and Sentinel-2 are affected heavily by the ice movement, prohibiting the subtraction of the winter mean (i.e. a different surface is observed unless the geometry is tracked in time) (Figures 4.3 and 4.6).
- In the Sentinel-2 classification, image edges and geometry induce steep gradients and cause false identification of channel segments due to the Gabor filter. Additionally, channel segments may be duplicated parallel to the channel orientation depending on the bandpass filter (Figure 4.5) and channel width w.
- The HH minimum is the most important feature. However, the GLCM contrast feature with its orientation parallel to the channel outweighs the other backscatter characteristics, indicating the potential benefit of including GLCM parameters (Table 4.2).
- The GLCM-based random forest regressor partially captures channels and is substantially outperformed by a Sentinel-1 HH-minimum thresholded classification (Tables 4.1 and 4.4).

4.2 Humboldt Glacier

This section encompasses the Humboldt Glacier study case and its results. Section 4.2.1 provides a reference Sentinel-2 channel delineation, which is compared with Sentinel-1 data and in Section 4.2.2. Finally, Section 4.2.3 gives the random forest regression results, followed by a summary of findings in Section 4.2.4.

4.2.1 Sentinel-2 Data and Delineation

Following Rawlins et al. (2023), the classification of a single Sentinel-2 image has been shown previously in Figure 3.2. An NDWI threshold of 0.4 to delineate large channels and bodies is taken, after which the path-opening algorithm is applied to enhance narrower channels. To acquaint ourselves with Sentinel-2 satellite images, consider Figure 4.11, providing reference images for the Sentinel-1 images in Section 4.2.2.

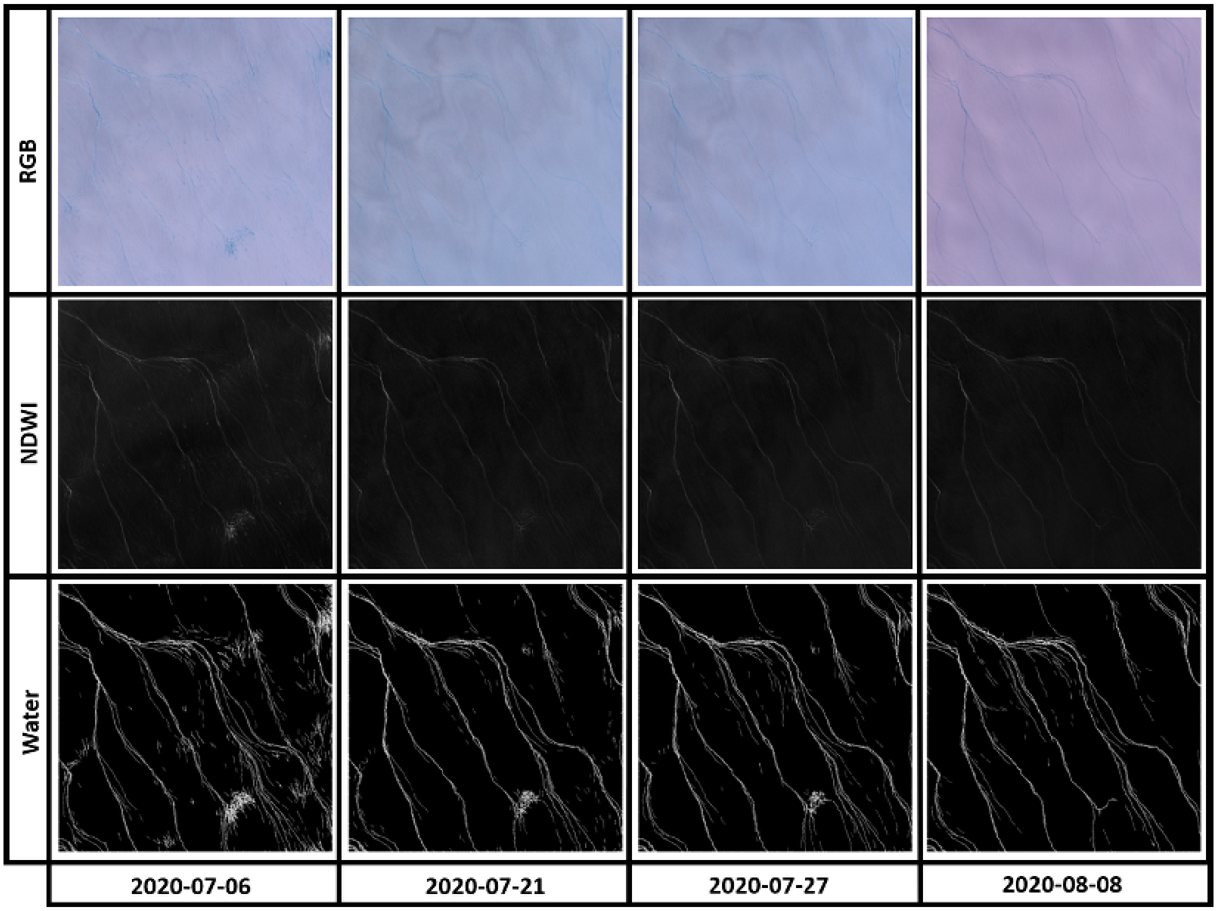

Figure 4.11: Subset of Sentinel-2 RGB (top), NDWI (middle) and water classification (bottom) images of the Humboldt study case taken between July and September 2020.

Classifying and stacking individual images results in Figure 4.12. Compared to the 79°N study case, ice movement is significantly less (0.1 m/d as opposed to 3.0 m/d), and channels appear not to be stretched. It is important to note that the spatial extent of the Humboldt study case is larger than that of the 79°N Glacier, resulting in a smaller relative displacement.

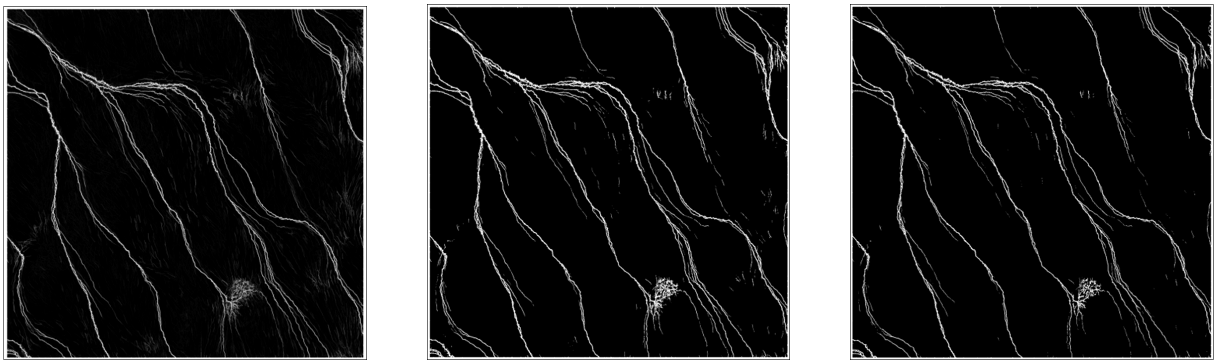

(a) Water fraction f_w [0-1]. (b) Classification ($f_w \geq 0.3$). (c) Classification ($f_w \geq 0.4$).

Figure 4.12: Sentinel-2 water classification of the Humboldt Glacier study area from June to September 2020. Fraction f_w corresponds to the fraction of images in which a pixel is classified as water.

4.2.2 Sentinel-1 Data and Comparison

Figure 4.13 shows Sentinel-1 scenes of similar dates to the Sentinel-2 images presented in Figure 4.11. Visual inspection elucidates the impression that the channels are partially visible at best from the Sentinel-1 data. Additional examination of band ratios shows no signs of improvement in channel visibility. Note that the visibility changes over time—in comparison to the NDWI from Sentinel-2, neither HH nor HV appears to retain the detail they do have over time. As such, hopes are shed on studying the seasonal evolution of the drainage network from individual Sentinel-1 images in a similar way to Rawlins' approach to Sentinel-2. Additionally, due to the speckly nature of Sentinel-1 noise, one cannot simply apply Yang's path-opening algorithm to, for example, the top left image of Figure 4.13. Granular textures induce steep gradients, obstructing the ability of the algorithm to identify linear features highlighted in Figure 4.14.

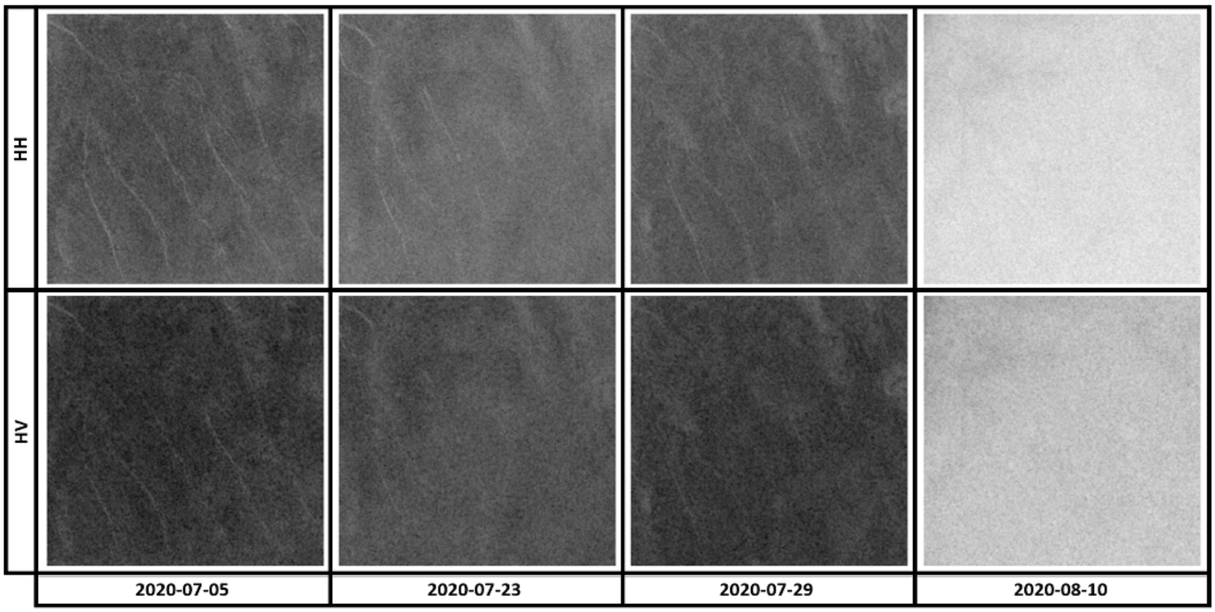

Figure 4.13: Subset of the Sentinel-1 HH-polarization (top) and HV-polarization (bottom) images of the Humboldt study case taken between July and September 2020.

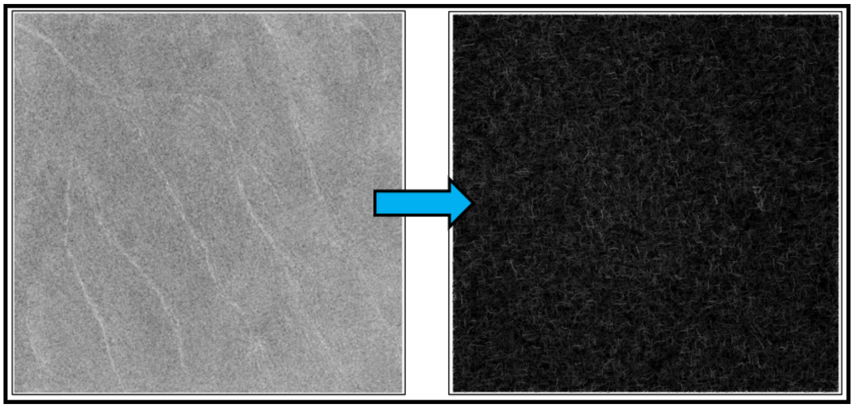

Figure 4.14: Yang's path-opening algorithm used on a Sentinel-1 HH-polarzied scene of July 5th, 2020.

Applying a similar backscatter threshold to differentiate between channels and surroundings as is done in Figure 4.5 reveals that the speckly nature of Sentinel-1 is also a limiting factor. The channels are classified as water correctly for the most part, though several segments remain absent. Figure 4.16 displays the composite images to attain a more complete picture.

Notice how the channels appear bright in the HH minima before subtraction, whereas they appear dark in the previous study case (Figure 4.6). Similarly, for the standard deviation, they appear dark here, whereas they appear (partially) bright for the 79°N Glacier compared to the surroundings. Zooming in on a channel segment on the HH standard deviation image from Figure 4.12 shows that while composite

Sentinel-1 images can capture channels to some extent, the precision is lacklustre compared to Sentinel-2. Figure 4.17 highlights that speckly noise persists even when considering multiple images.

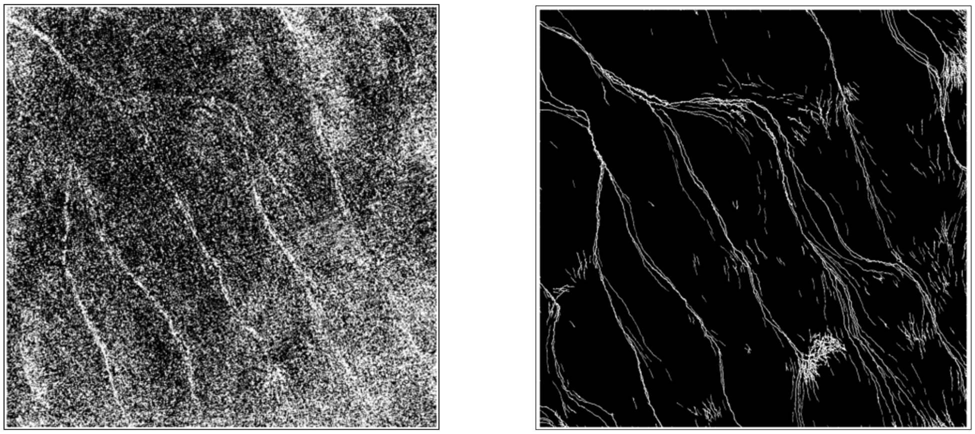

(a) Sentinel-1 thresholded ($t = -15$ dB) water classification of 2020-07-05.

(b) Sentinel-2 reference water classification of 2020-07-06.

Figure 4.15: Comparison of Sentinel-1 thresholded classification and reference Sentinel-2 classification of the Humboldt Glacier study case.

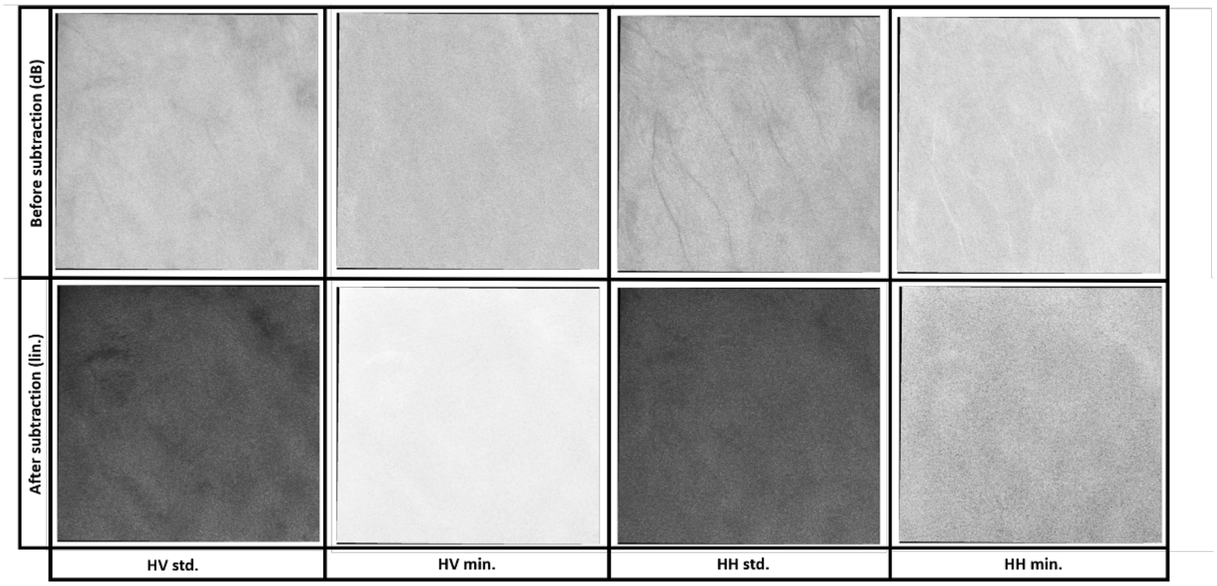

Figure 4.16: Co- and cross-polarized Sentinel-1 backscatter minima and standard deviations from June to September 2020 on the Humboldt Glacier study area before (dB units) and after (linear units) subtraction of the winter mean.

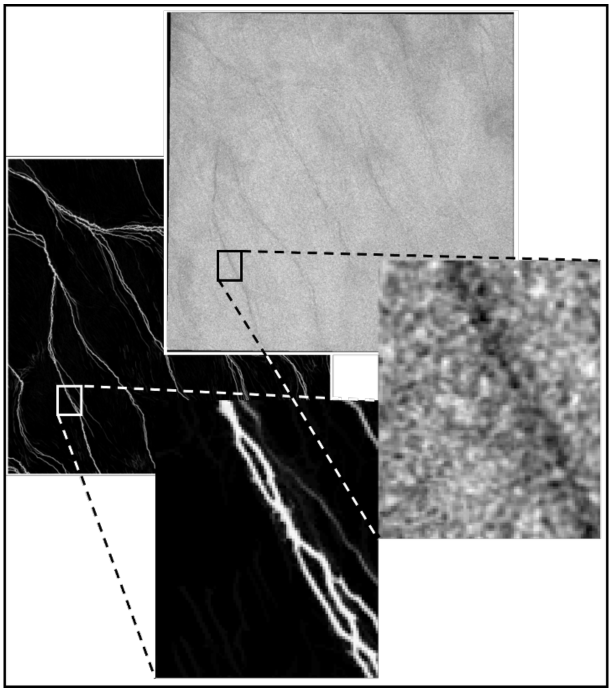

Figure 4.17: Humboldt Glacier zoom in on Sentinel-2 classification and the HH standard deviation image of Sentinel-1.

While the spatial alignment of meltwater features appears mostly correct, it remains challenging to construct a smooth channel from the Sentinel-1 data at a pixel-level feature size as the pixels themselves do not coincide perfectly.

4.2.3 Random Forest Regression

Taking 5000 samples for each of the classes, including the transition pixels described in Section 3.2 ($f_w > 0.4$ for water), computing the GLCM parameters and training two random forest regressors with the maximum NDWI and water fraction as targets, the results are insignificant. The maximum NDWI is included purely for experimental reasons since using the water fraction f_w provided meaningless results.

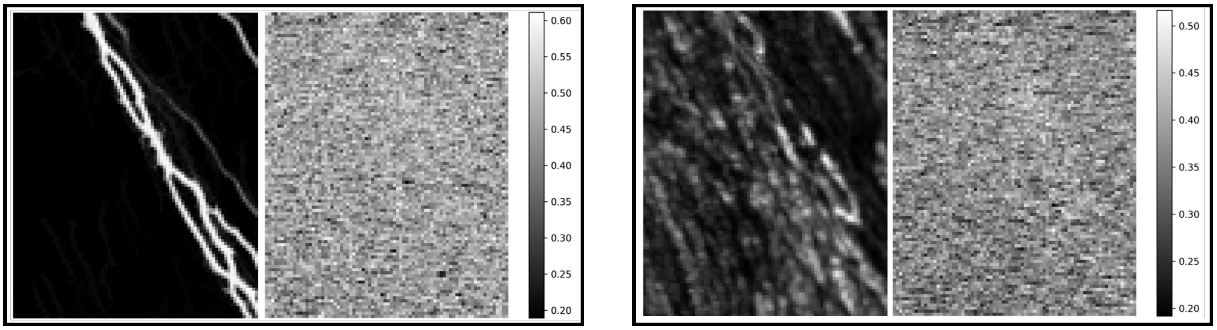

(a) Random forest model results (right) with water fraction (left) as the target variable.

(b) Random forest model results (right) with maximum NDWI (left) as the target variable.

Figure 4.18: Random forest model results for a small subsection when trained on 5000 water, transition and other samples with GLCM properties on the Humboldt Glacier study case.

As seen in Figure 4.18, neither model provides meaningful results. This is most likely due to the minor misalignment between pixels visible in Figure 4.17, causing automated random sampling of pixels based on Sentinel-2 not to represent their true classification for Sentinel-1. In both cases, feature importance given in Table 4.5 serves as confirmation.

	Feature Importance per Target Variable	
Feature	Water fraction f_w	Maximum NDWI
HH std.	0.08286	0.03819
HV std.	0.02294	0.01996
HH min.	0.01936	0.02332
HV min.	0.01618	0.02328
Correlation	0.01714	0.01758
Contrast	0.01173	0.01265
Dissimilarity	0.00822	0.00856
Homogeneity	0.01658	0.01716

Table 4.5: Comparison of feature importances across two random forest models trained on the Humboldt Glacier study case. GLCM properties are averaged across angles.

Correlation, contrast, dissimilarity and homogeneity are averaged over the angles and polarization properties. However, none of the individual combinations (e.g. correlation of HH standard deviation at 0 degrees) significantly outweighed the backscatter statistics. Note that the importance of the HH standard deviation matches the observations in Figure 4.16, supporting that it remains the most important feature amidst the spatial misalignment. Overall, the feature importances are low, and the regression appears randomized in both cases.

4.2.4 Summary of Findings

Summarizing the findings of this study case, consider the following:

- Compared to the previous study case, the bright-dark backscatter contrast is inverted. Channels appear bright (higher backscatter) compared to the dark (low backscatter) background (Figures 4.4, 4.6, 4.13 and 4.16).
- Small channels are captured partially, at best, by individual Sentinel-1 images (Figure 4.15).
- Yang's path-opening algorithm requires adjustment to speckle noise and possibly other phenomena to be suitable for Sentinel-1 data (Figure 4.14).
- Subtracting the winter mean eliminates the contrast between the background and channels almost completely (Figure 4.16).
- While channels are visible from composite Sentinel-1 images, the spatial alignment at a pixel-level scale is problematic for the random sampling approach (Figure 4.17).
- The random forest regression appears random and is likely a result of the spatial misalignment, sampling approach and persisting speckle noise (Figures 4.17 and 4.18).

4.3 Russell Glacier

This section encompasses the results of the Russell Glacier study case. Section 4.3.1 employs the Sentinel-2 classification scheme and produces a reference classification, followed by Section 4.3.2, which compares the Sentinel-2 outcome to Sentinel-1 data. Thereafter, Section 4.3.3 zooms in on a small subsection and performs random forest regression. Finally, Section 4.3.4 summarizes the findings of this study case.

4.3.1 Sentinel-2 Data and Delineation

The classification scheme in Figure 3.1 is followed to delineate water from Sentinel-2 images. Figure 4.19 shows RGB, NDWI and corresponding classification images taken at different times throughout July and August of 2019 as reference for the upcoming Sentinel-1 images.

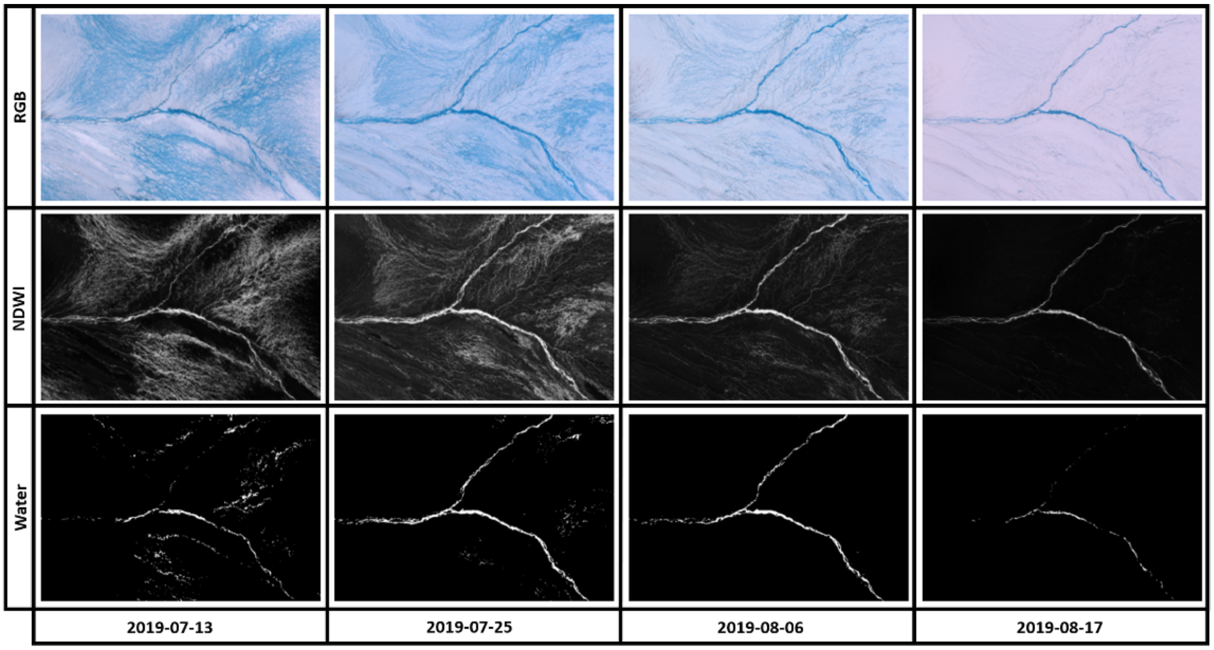

Figure 4.19: Subset of Sentinel-2 RGB (top), NDWI (middle) and water classification (bottom) images of the Russell study case taken between July and September 2019.

The images from July 13th and July 25th show that blue ice or slush is removed from the classification, whereas the channels remain. For the images from August, however, parts of the channel start to disappear while they are still visible from the NDWI images. Stacking the images and applying various thresholds f_w to delineate meltwater results in Figure 4.20.

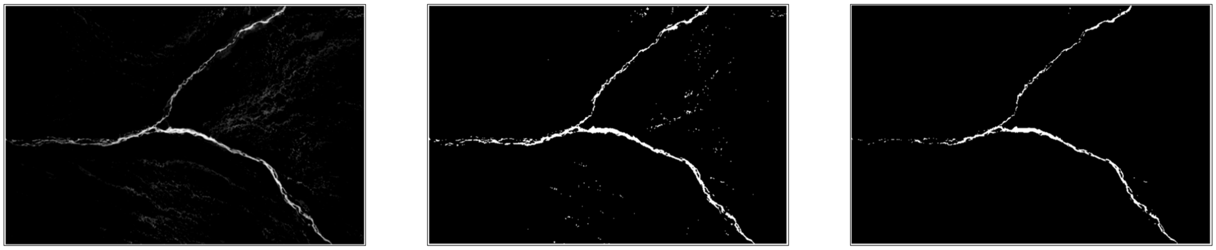

(a) Water fraction f_w [0-1]. (b) Classification ($f_w \geq 0.2$). (c) Classification ($f_w \geq 0.3$).

Figure 4.20: Sentinel-2 water classification of the Russell Glacier study area from June to September 2020. Fraction f_w corresponds to the fraction of images in which a pixel is classified as water.

As mentioned, most of the channel is delineated appropriately, while most blue ice or slush is not classified as water. Comparison of Figure 4.20b and 4.20c shows that decreasing fraction f_w leads to a tradeoff between the completeness of the channel delineation and the inclusion of blue ice or slush. However, for a channel-oriented reference classification, the classification scheme delivers adequately.

4.3.2 Sentinel-1 Data and Comparison

Comparing Sentinel-2 images from Figure 4.19, Figures 4.21 and 4.22 show Sentinel-1 images of similar dates before and after subtracting the winter mean.

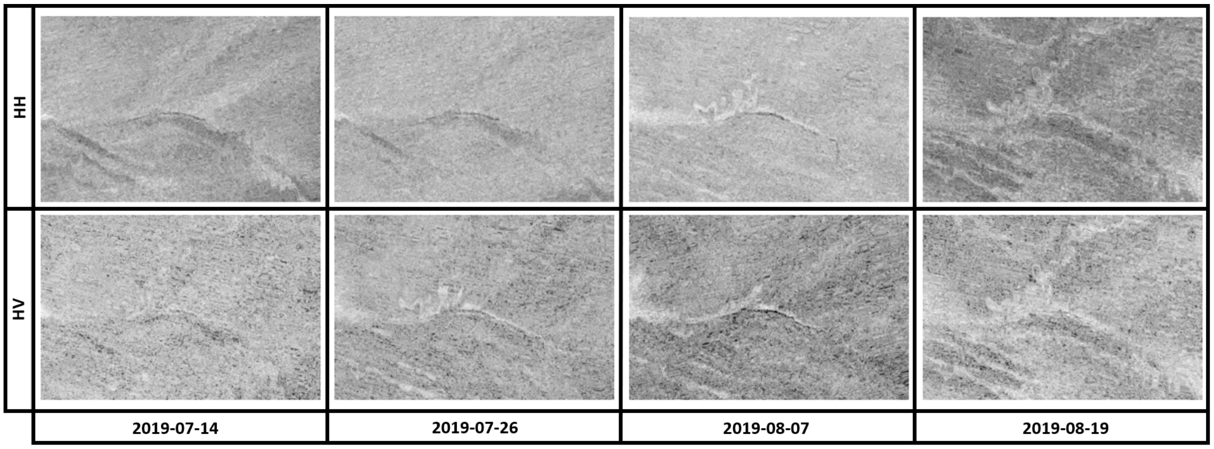

Figure 4.21: Subset of the Sentinel-1 HH-polarization (top) and HV-polarization (bottom) images of the Russell study case taken between July and September 2019 without subtraction of the winter mean.

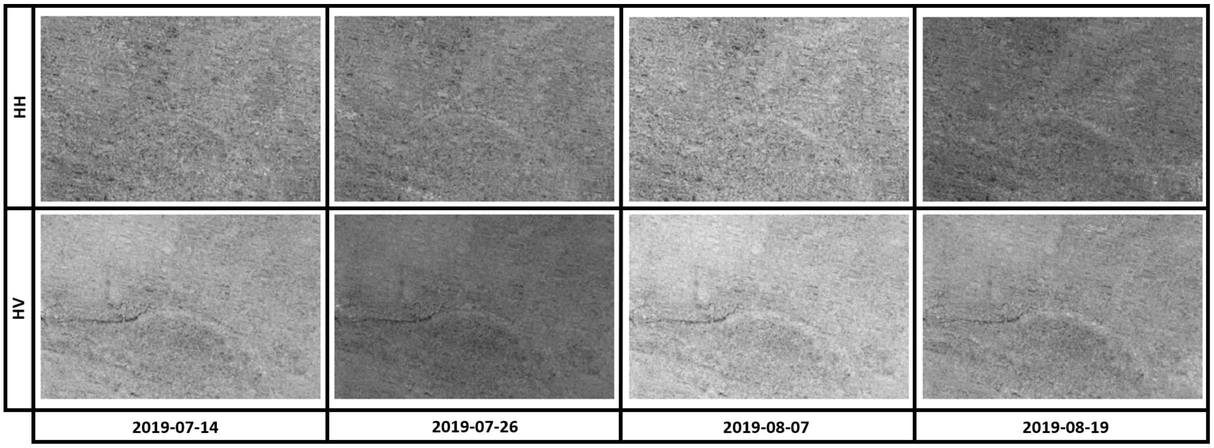

Figure 4.22: Subset of the Sentinel-1 HH-polarization (top) and HV-polarization (bottom) images of the Russell study case taken between July and September 2019 with subtraction of the winter mean.

Similar to the Humboldt study case, channels are partially visible in individual Sentinel-1 images. Furthermore, the Northward branch of the bifurcation remains mostly invisible, whereas the Southward branch has some visibility. Interestingly, subtracting the winter mean results in a low HV backscatter of the channel on the left of each image, while the contrast inverts right around the bifurcation. Overall, it appears that subtracting the winter mean benefits HV-polarized backscatter the most, seemingly reducing the background speckle upon visual inspection. It is doubtful whether subtraction of the winter mean is helpful for HH-polarized images in this study case as it seemingly loses detail around the channel. Recall that for this study case, ice movement was in the order of 0.5 metres a day.

Figure 4.23 provides the composite Sentinel-1 images when mapped onto an arbitrary reference profile from one of the Sentinel-1 images. The northward branch of the bifurcation remains almost entirely invisible across all images, whereas the remainder of the channel can be delineated approximately with the eye.

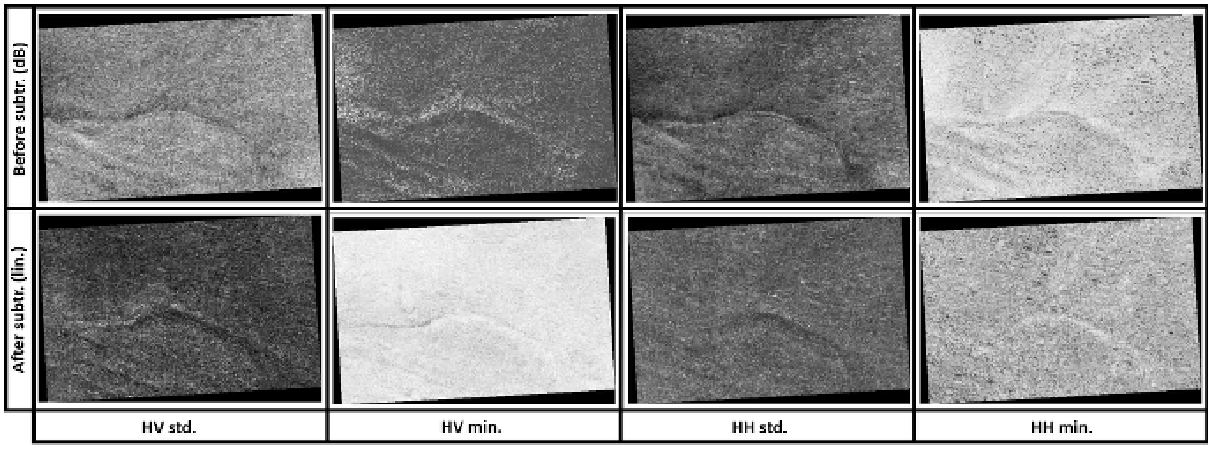

Figure 4.23: Co- and cross-polarized Sentinel-1 backscatter minima and standard deviations from June to September 2019 on the Russell Glacier study area before (dB units) and after (linear units) subtraction of the winter mean.

4.3.3 Random Forest Regression

Similar to the other study cases, a small subsection is provided in Figure 4.24. As the channel is visible in both series of images regardless of whether the winter mean is subtracted, both are used for GLCM property calculations and fed into the random forest regressor, totalling $2 \times 68 = 136$ input features. Figure 4.25 gives the random forest regression results with the water fraction as the target variable with 3000 samples per class. Fewer samples are taken rather than 5000 due to the doubled amount of calculations for the GLCM properties. Pixels are considered to be water if $f_w > 0.25$.

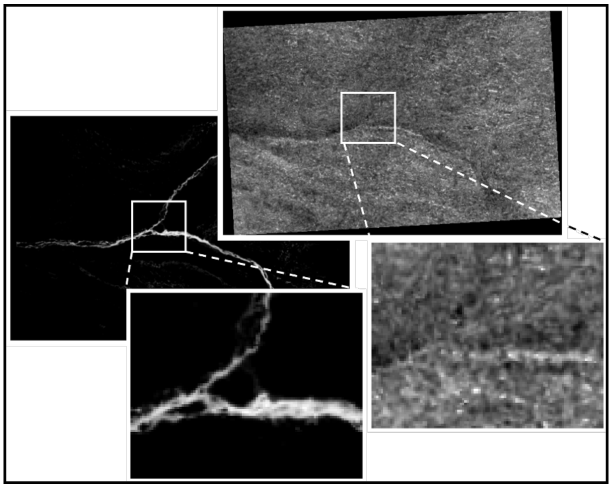

Figure 4.24: Russell Glacier zoom in on Sentinel-2 classification and the HH standard deviation image without subtraction of the winter mean of Sentinel-1.

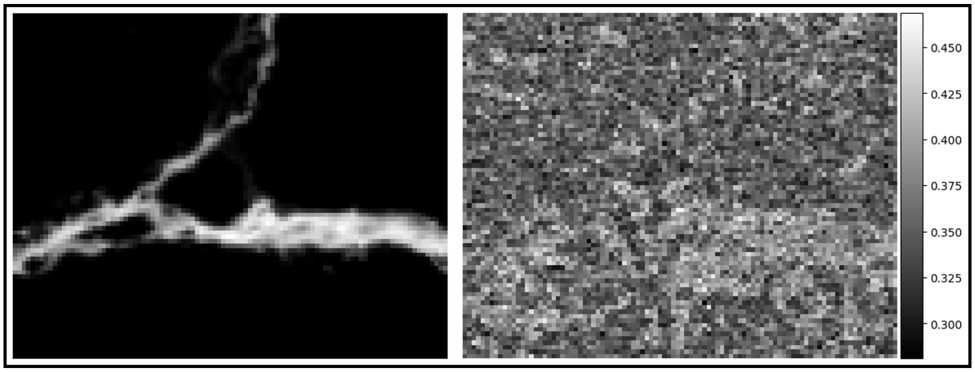

Figure 4.25: Russell Glacier subsection random forest regression results using GLCM properties of composite images with and without subtracting the winter mean with water fraction (left) as the target variable.

Unfortunately, similar to the Humboldt study case, the outcome yields no promising results. At best, there is a hint of a channel on the right-hand side of the subsection.

Feature	Importance
HH std. (f)	0.11767
HH min. (f)	0.04100
HV min. (f)	0.03971
HH std. (r)	0.03437
HV std. (f)	0.02804

Table 4.6: Top 5 features based on feature importance of the Russell Glacier study case. The (r) and (f) represent the inclusion and subtraction of the winter mean, respectively.

Feature	Importance
HH min. (f)	0.04100
HH std. (f)	0.11767
HV min. (f)	0.03971
HV std. (f)	0.02804
HH min. (r)	0.00851
HH std. (r)	0.03437
HV min. (r)	0.00744
HV std. (r)	0.00714
Correlation	0.00584
Contrast	0.00582
Dissimilarity	0.00426
Homogeneity	0.00647

Table 4.7: Feature importance summary of the Russell Glacier study case. GLCM properties are averaged across angles across angles.

The randomness is reflected in the feature importance, where none other than the HH standard deviation of the winter mean subtracted images have negligible importance. Additionally, the effect of the GLCM property addition is insignificant.

4.3.4 Summary of Findings

To address the findings of this study case, the following is constituted:

- The Sentinel-2 classification scheme effectively removes (most of) the blue ice and slush from the water classification (Figures 4.19 and 4.20).
- From both individual and composite Sentinel-1 images, one can see a bright-dark backscatter inversion, rendering thresholding techniques ineffective (Figures 4.22 and 4.23).
- While the Southern branches of the channel can be distinguished in individual and composite Sentinel-1 scenes, the Northern branch remains mostly invisible to the eye. This highlights that Sentinel-1 is not able to capture the same water as Sentinel-2.
- Subtraction of the winter mean appears to have little effect visually (Figure 4.23). On the other hand, subtraction of the winter mean seems to help the random forest regression (Table 4.6). However, this may not be justified, considering the overall quality of the regression results.

5. Discussion

While the results have been discussed and summarized mostly, this chapter provides further elaboration. Furthermore, they have revealed limitations and problems regarding the methodology, which need to be attended to. Section 5.1 reflects upon the approach in hindsight and states the encountered issues, whereas Section 5.2 delves into the results of each study case once more to summarize and add onto previous statements. Section 5.3 comments on the relevance of Sentinel-1.

5.1 Revisit: Methodology

Revisiting the iterative process that formed the methodology, the results indicate that the approach relies on some unrealistic assumptions. Moreover, certain problems are intentionally disregarded, as they could not be fixed within the timeframe of the study. These issues are discussed here and partially forwarded to the recommendations to raise awareness. Summarizing the most critical points:

1. Movement of ice is ignored.
2. The Sentinel-2 reference classification is assumed to be correct.
3. Sentinel-1 and Sentinel-2 data are assumed to align perfectly spatially.
4. Persisting speckle noise in composite images.

Ice movement is mostly ignored throughout this study, although it significantly impacts two crucial aspects. Calculating the minimum and standard deviation of a pixel implies that, over time, that pixel within the predefined geometry refers to a static point on the glacier surface. When ice movement is considerable, as seen in the 79°N study case, channel segments appear elongated parallel to the direction of ice flow in composite images. This can lead to overestimating surface area melt. Consequences have been partially avoided by selecting two study cases (Humboldt and Russell) where ice movement is less pronounced (Section 2.6). Ice movement affects both the compositing of images and the ability to subtract the winter mean. Taking the exact spatial coordinates at different times will represent two different surfaces as a result of ice flow. To mitigate this, appropriate georeferencing techniques should be employed—ice movement must be compensated for by calculating the relative displacement pixel-per-pixel between images. The spatial and temporal heterogeneity of ice flow makes this a challenging task, especially when the features may be of pixel-level scale.

Incorrect Sentinel-2 reference classification is a limiting factor of the random forest approach. As seen in Figure 4.5b, channel segments on the 79°N Glacier are duplicated parallel to their direction as an artefact of the bandpass filter and width parameter w. Due to the varying widths of the channels on the 79°N Glacier, adapting w for one channel will have drawbacks for the other. In general, the path-opening algorithm results are highly affected by its parameters and should be optimized for each study case. Additionally, the edges form steep gradients for the Gabor filter, resulting in false water classification. To mitigate the latter, images are cropped before drawing samples to exclude pixels near the edges. The former can be minimized by experimentally determining the bandpass filter frequencies for each study case. Finally, the morphological path-opening step opens and closes segments, potentially removing water pixels to enhance connectivity and smoothness. A false Sentinel-2 classification directly affects the quality of the random forest model, as the pixel water fraction is taken as the target variable. Misidentifying water and non-water pixels reduces the effectiveness of the random forest regression, as two pixels may share similar features but have different targets.

Spatial alignment of Sentinel-1 and Sentinel-2 is crucial since samples are drawn randomly by index. To improve spatial alignment, all images are mapped to a reference profile. However, as seen in Figure 4.17, the Sentinel-1 data (still) does not perfectly coincide with Sentinel-2. In GEE, radiometric terrain flattening is not applied, and the terrain correction (orthorectification) converts data to ground range geometry without considering the terrain. This likely induces minor misalignment of pixels, which is problematic specifically for features at a pixel-level scale. Misalignment affects the random forest regression, most noticeably in the results of the Humboldt Glacier study case (Figure 4.18). This is discussed further in the recommendations.

Speckle noise persists even when considering composite images, highlighted by Figures 4.7, 4.17, and 4.24. In terms of GLCM texture features, this is particularly problematic as the 3-by-3 patch may inherit a large variance. Due to this, similar patches may be characterized by different texture features, posing problems for the regressor as two highly varying feature combinations can share a similar target. Based on the current methodology and results, one cannot confirm whether this speckle noise in composite images originates from the nature of Sentinel-1 data, from ice movement, or from potentially inadequate preprocessing in Google Earth Engine.

In addition to these, there are a few concerns regarding the random forest regression and GLCM properties. Hyperparameters for the random forest regressor have not been optimized due to the poor regression results and would likely not have changed the undesirable outcome. While regressing to per-pixel water fraction is more flexible than a binary distinction and omits false identification to some extent (assuming it does not occur regularly), it is not directly related to the input data. The backscatter minimum should rather be used for a binary distinction, whereas the standard deviation is a measure of change, neither of which resembles the fraction of images in which pixels are classified as water. Furthermore, including transition pixels when spatial alignment is imperfect may reduce the quality of the results. Pixels adjacent to water pixels are arguably the most confusing, as this is precisely where misalignment is consequential. In hindsight, purposely excluding these regions may have been advantageous.

Moreover, GLCM properties are calculated over a distance of 1 pixel. Figures 4.7, 4.17, and 4.24 highlight that the speckly nature of data persists when compositing. Noise introduces large variability within the GLCM parameters, especially at small-scale features such as channels. This reduces their effectiveness in image segmentation via the random forest regressor as the kernel over which the GLCM parameters are calculated does not encapsulate channels exclusively. Surrounding background may also be included for small-scale features, reducing the texture feature uniqueness for water and non-water pixels.

In general, the GLCM texture feature clustering shown in Figure 3.3 is heavily affected by speckle. The examples from the figure are picked manually for illustration purposes, but taking other examples may have a very different result displayed in Figure 5.1. Clustering techniques (e.g. K-means or Hierarchical clustering) should be explored to examine whether the two different classes clump together, or perhaps the analysis would suggest the presence of another class, such as the transition pixels.

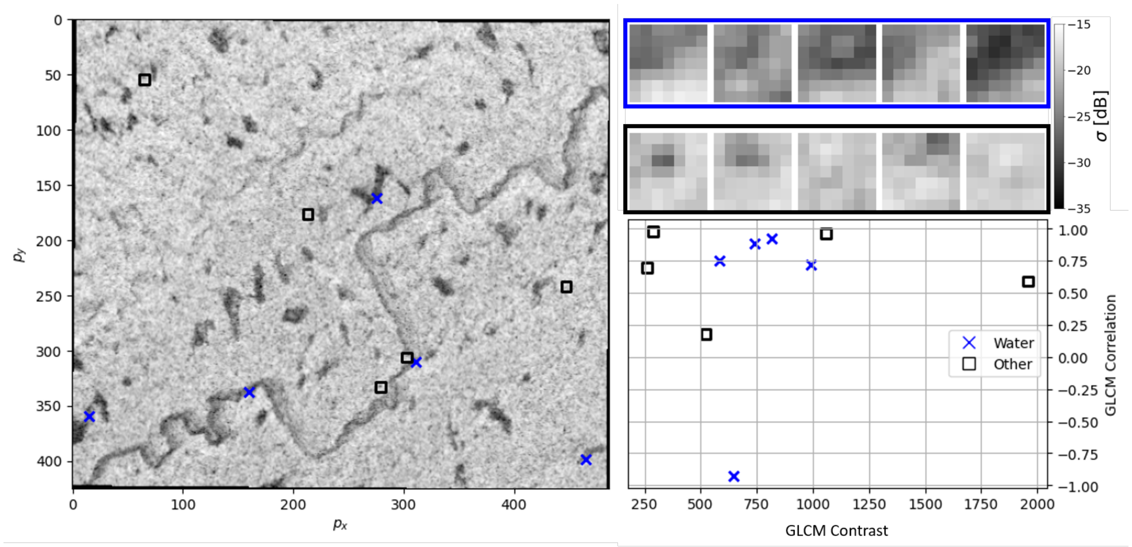

Figure 5.1: GLCM texture features for different surface patches similar to Figure 3.3. Note how water patches and non-water patches no longer appear to be grouped as much based on these GLCM texture features.

As seen in Figure 5.1, water and other pixels tend to overlap in the 2-dimensional feature space of contrast and correlation. Extending this to include all samples, Figure 5.2 highlights that overall, water pixels tend to have higher contrast, though the correlation appears to be similar for both classes.

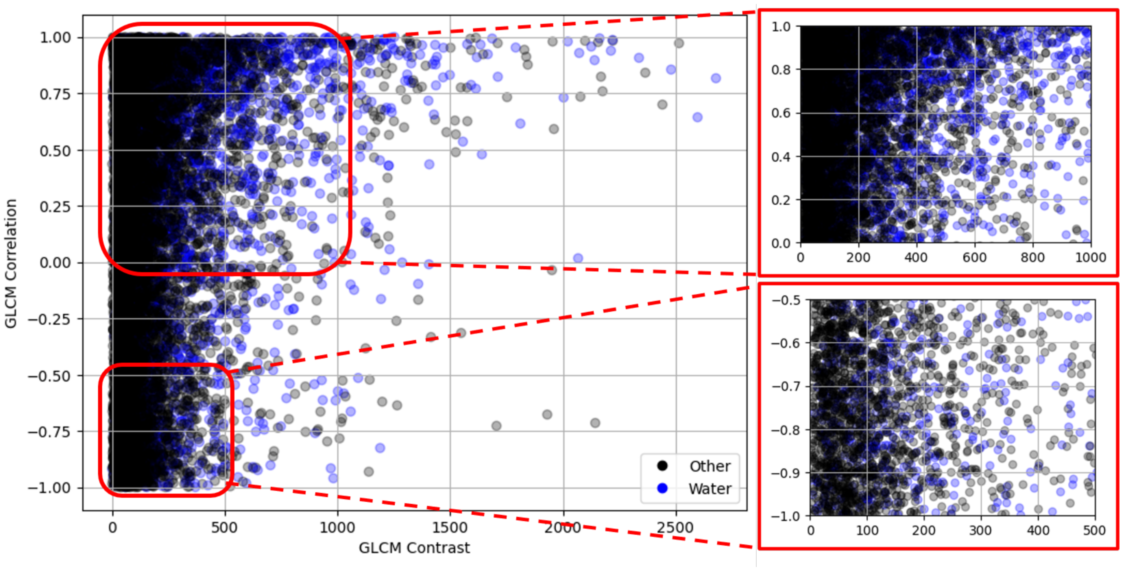

Figure 5.2: 2D GLCM texture feature space using contrast and correlation for all samples. Zoom-ins show that water pixels gravitate to higher contrast values.

Note that this is a 2D representation of a 68-dimensional feature space, which can be extended to any pair of features to determine whether a unique combination of features results in clear clusters. The combination shown above, given by HH min. contrast at 45 degrees and HH min. correlation at 135 degrees, shows the greatest separation of cluster means within a 2D feature space.

In an attempt to identify a suitable number of classes, the elbow method using cluster inertia of K-means clustering is shown in Figure 5.3. The number of clusters k ranges from 2 (i.e. water and other pixels) to 7. Feature weights are taken to be equal and weighted, where the weight of GLCM texture features is 1/16, corresponding to 4 angles times 4 features per backscatter image. The weights of the backscatter images themselves are kept to 1.

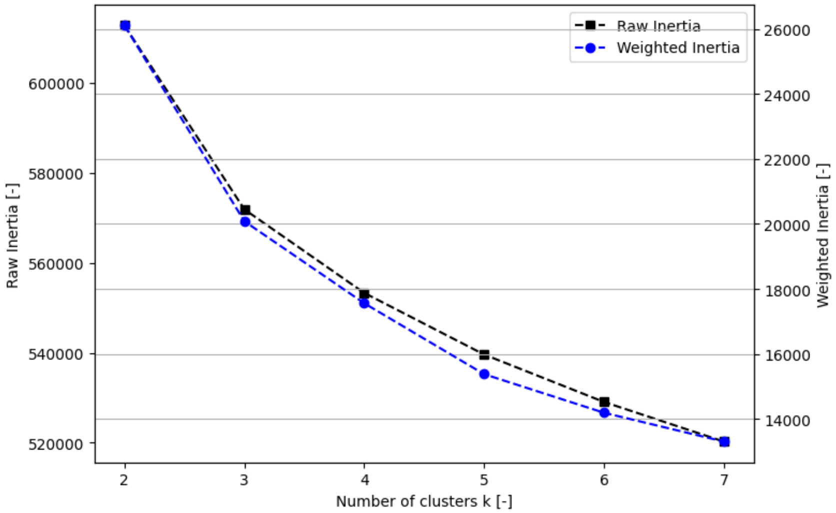

Figure 5.3: Cluster inertias for k clusters with equal-weight features and weighted features, where the weighted features are 1 for backscatter images and 1/16 for texture features.

Unfortunately, no elbow (number of clusters where the decrease in inertia stagnates) is present for either inertias. In general, there is limited change when weighing features, indicating that their inclusion barely improves clustering. The current implementation of the GLCM texture feature calculations is approximately 700 px/min on Google Colab. For images with 10-by-10 metre resolution, this translates to a processing speed of roughly 14 min/km^2, which is incredibly limiting in terms of scalability. As such, they cannot be computed within a reasonable amount of time and used to perform clustering for the entire image.

5.2 Assessment of Results

Assessing the three study cases based on their results and relating them to the research questions, the approach showed the most promise in the 79°N Glacier study case despite the interference of ice movement and artefacts. Individual Sentinel-1 scenes are able to capture the main channel and meltwater ponds, whereas the secondary channel was captured partially. Examination of the DEM in Figure 2.4a shows that the surface does not slope in the direction of the channel, likely resulting in a relatively smooth and flat surface and enabling specular reflection of the water surface. Composite images suffer from ice movement, and as such, the quality of input data for the random forest regression degrades. However, feature importance reveals that despite this, the contrast of the HH standard deviation at a 45-degree angle outweighs the polarimetric data other than the HH minimum. This approximately coincides with the channel orientation, indicative of its potential. Unfortunately, the results of the random forest regression are worse compared to the classification based on thresholding the HH minimum, seen in Figure 4.10 and comparison of Tables 4.1 and 4.4. The specular reflection of the water surface results in low backscatter values for the main river, whereas the narrower channel has mixed backscatter values. A possible explanation is that the ground resolution is not high enough, resulting in pixels that contain more than one surface element. For example, a 10-by-10 metre GRD (5-by-20 metre SLC) pixel may contain part of the channel and surrounding ice and snow. All elements in a pixel contribute to the measured backscatter, resulting in intra-pixel heterogeneities and a complex interpretation which may not be representative of water.

The Humboldt Glacier study case supports these findings, highlighting that channels are captured partially in individual images. Channels appear to have larger backscatter than the surrounding snow and ice, contrary to those in the 79°N Glacier study case (Figures 4.6 and 4.16). Various factors may cause this inversion, such as surface roughness, liquid water content and snow/ice density. The complex interaction between microwaves and (partially molten) snow influences the appearance of channels with respect to their surroundings. The composite images (Figure 4.16) show that the standard deviation of the channels is rather low compared to the surroundings, indicating relatively constant channel surface properties over the melt season. Note that this is highly dependent on the timeframe of the study case—in case the channels are liquid from start to end, a low standard deviation is expected, whereas a full melting cycle would inherit drastic changes in intensity. Minimum backscatter, on the other hand, appears to be higher than that of the surroundings but remains difficult to attribute to a source. Unfortunately, the spatial alignment at a pixel-level scale, in combination with the persisting speckle noise, takes a toll on the random forest regression results. While channel delineation can be done by hand based on the Sentinel-1 data, using Sentinel-2 as an exact reference resulted in a randomized classification. Using the maximum NDWI as an alternative target for the regressor does not improve the results, which could be anticipated by inspecting the target image of Figure 4.18b. The inclusion of transition pixels (Section 3.2.3) may have reduced the results. Subsequent analysis should follow, excluding them during training.

The Russell Glacier study case portrayed the aforementioned bright-dark contrast transition in individual and composite Sentinel-1 images. Adding on to the previous reasons that may cause this, terrain and shadows should also be mentioned. For the Russell study case, the terrain profile slopes downward with approximately 50 metres across 5 kilometres from East to West, a similar inclination to that of the Humboldt study case. A relatively steep drop in height is present in Figure 2.4c, located on the Southward branch of the channel. Relating this to individual Sentinel-1 images with the winter mean subtracted, Figure 4.22 shows that it coincides with the bright-dark inversion. Complex terrain characteristics create different surfaces of similar backscatter intensities and make thresholding techniques for Sentinel-1 unfeasible to delineate the channel. The GLCM-based random forest regression proves to be no viable option either, as the results appear to be random (Figure 4.25). It is important to note that the Northward branch of the channel remains mostly invisible in all composite Sentinel-1 images given in Figure 4.23, highlighting yet again that some channel segments are not contained within the data. The Sentinel-1 orientation and view angle may be such that the line of sight is obstructed, leaving the channel undetected. Nevertheless, these pixels may be used to train the random forest regressor due to the random sampling approach. Ultimately, this reduces the quality of the regression results as the corresponding Sentinel-1 data reveals no unique patterns compared to the surroundings in this area. The random forest results remain difficult to assess due to speckle and misalignment, and it is inconclusive whether subtraction of the winter mean would increase the regression quality.

5.3 Relevance of Sentinel-1

With the goal of mapping supraglacial drainage networks in mind, the findings show that larger channels (and water bodies) can be delineated successfully by thresholding. Narrow channels, on the other hand, are not visible from individual Sentinel-1 scenes and may remain invisible even when compositing. The path-opening approach described by Yang et al. (2015) allows channels to be enhanced from Sentinel-2 imagery, however, no similar techniques exist for Sentinel-1 data. While Sentinel-1 provides information on buried lakes, it cannot be used to attain a full picture of the drainage network (Zheng et al., 2023). Despite the advantage of having a constant flux of data, the data itself does not contain the small-scale detail necessary for narrow channel delineation. As such, Sentinel-2 remains to be the better-suited satellite for the purpose of delineating the drainage network. An increase in spatial resolution would justify a revisit to this topic. To further assess the limitations of Sentinel-1, other machine learning methods such as convolutional neural networks and U-nets should be explored. Transfer learning on networks originating from a civil engineering background designed for crack detection could be promising. This is elaborated upon in the recommendations.

6. Conclusion

The analyses conducted throughout this thesis have mainly given qualitative insights regarding the feasibility of using Sentinel-1 for supraglacial channel delineation. While the quality of random forest regression is quantified in terms of accuracy, precision, recall and F1 score, this merely concerns the Sentinel-2 reference classification. The reference classification suffered from imperfections, and as such, these metrics may not represent the actual potential of both the approach and the inclusion of Sentinel-1. Furthermore, the training data suffered from spatial misalignment induced by a combination of glacier flow and possibly inadequate data preprocessing. Ultimately, this has degraded the quality of both the input parameters and the target variables. Revisiting the research questions, consider the following as contributions to the answers:

- **To what extent can Sentinel-1 data be used to identify supraglacial channels?**
  Channels with sufficient cross-sectional area appear in both co- and cross-polarized data in individual Sentinel-1 scenes. Narrower channels approaching the pixel resolution of 10 metres tend to disappear, likely due to the heterogeneity of elements within pixels (i.e. a combination of water, snow and ice). However, other study cases have shown that channels are captured partially in individual scenes. Compositing images by taking the backscatter standard deviation (reflecting change) and minimum (expected to correlate with water presence) provides a more complete picture. Areas with complex terrain structures and narrow channels may result in higher backscatter values for water surfaces compared to the surrounding features, potentially inversing the bright-dark contrast. The inversion remains difficult to attribute to a source as many factors may contribute, including but not limited to pixel heterogeneity, flow dynamics, and surface characteristics (e.g. density, surface roughness and liquid water content). Moreover, the Russell study case has shown that a channel captured by Sentinel-2 remained invisible in Sentinel-1 data. Finally, subtracting the winter mean has been shown to both diminish and enhance the contrast between channels and their surroundings case-dependently.

- **What are the challenges of using Sentinel-1 for supraglacial channel delineation?**
  The primary challenge of using Sentinel-1 is speckle noise contamination. Composite images were anticipated to reduce its impact, though the results have shown that it persists. Compared to Sentinel-2, which typically results in smooth channel delineation, binary classification results are characterized by granular textures for both thresholding and random forest regression. Furthermore, compositing images to attain a complete picture of the supraglacial drainage network introduces another problem—glacier flow causes meltwater features to be elongated in the direction of movement. Therefore, ensuring the spatiotemporal alignment of individual pixels is crucial to determining surface meltwater area accurately. With regard to the subtraction of the winter mean, it is important to note that throughout this thesis, ice movement has been ignored, rendering conclusions on the effectiveness debatable. In slow-moving areas, it showed potential despite poor regression results.

- **What value do thresholding and GLCM-assisted random forest regression add in this context?**
  Thresholding backscatter in individual Sentinel-1 scenes is promising but context-dependent. It has outperformed the GLCM-assisted random forest regression quantitatively in the 79°N Glacier study case and qualitatively based upon visual inspection of the Humboldt Glacier study case. However, due to the challenges and limitations of the approach addressed previously, the regressor is hindered significantly. Moreover, GLCM texture features are susceptible to variance within the 3-by-3 window caused by speckle noise, reducing their contribution to the regressor. Despite the persisting speckle and apparent misalignment, the feature importance has revealed that one of the GLCM parameters oriented parallel to the channel outweighed backscatter minima and variance. As such, arguments supporting the inclusion of GLCM parameters cannot be discarded. However, the current implementation is prohibitively expensive computationally, leading to an unscalable product. Further optimization and cluster analysis should be done to justify the use of GLCM texture features to delineate supraglacial channels.

7. Recommendations

Considering the extensive discussion on the methodology in Section 5.1 and the conclusions in Chapter 6, many suggestions can be made to potentially improve the results. They are summarised in three categories to be concise and highlight the most important recommendations.

Expansion on Sentinel-1 Data

While HH and HV polarized data are used to apply thresholds and obtain input features for the random forest regressor, the band ratio HH-HV (dB) is yet to be utilized. In terms of input features, an additional 2 (minimum and variance) $+ 2 \times 4$ (texture features) $\times$ 4 (angles) $= 34$ could be included. Whether these would improve the model performance is questionable, as most features showed minimal feature importance, although the band ratio might be valuable. The band ratio was used by Murashkin et al. (2018) to delineate leads (elongated areas of open water or thin ice resulting from ice fracturing) and is especially effective for areas with thin ice (Liang & Liu, 2020). On top of that, experimentally including the band ratio could provide insights regarding its applicability for supraglacial channel delineation. Furthermore, change detection algorithms could also be examined rather than using the backscatter minima and standard deviations. With the seasonal melting and refreezing cycle of water bodies and channels, employing a change detection algorithm may be beneficial in addition to the extremes and temporal variance. Moreover, it may help identify the moment surface melt and refreezing occurs, possibly enabling Sentinel-1 to study the seasonal evolution of supraglacial drainage networks.

Withdrawing ourselves from machine learning and change detection, adapting the path-opening algorithm to comply with Sentinel-1 data could be explored. Fundamentally differing filtering techniques would be required as Sentinel-1 data is subject to speckle noise, whereas Sentinel-2 data is not. The bandpass filter must be adjusted as the background is no longer characterized by low-frequency noise but by speckle noise. The Humboldt study case has shown that manual delineation of channels from Sentinel-1 is possible. However, their appearance is not as smooth as that of Sentinel-2. Even though the morphological path-opening step opens and closes segments, partially smoothing the channels, the granular texture would result in irregular gradients scattered around the channel. As such, it is sensible to include an additional smoothing step before subjecting the image to the path-opening algorithm. Essentially, either the input image must be of a similar nature texture-wise compared to the NDWI, or the algorithm must be adapted to handle speckle noise.

Speckle Noise and Misalignment

Speckle noise and misalignment have continuously degraded the quality of input features and target variables. Their source remains challenging to identify as it may have a multitude of possible contributors. As stated, the Google Earth Engine preprocessing skips specific steps, Sentinel-1 speckle noise is unavoidable, and ice movement has been ignored throughout this study. Speckle filters have purposely been omitted to maintain as much pixel-scale detail, and study cases with limited velocity magnitudes have been examined to mitigate these factors to some extent. However, the potentially deficient preprocessing has not been addressed. Due to limited allocatable time (and perhaps the delayed realization), attempts at correction have not been made. A suggestion is to perform the preprocessing in the Sentinel Application Platform (SNAP), which includes more precise terrain correction, and compare the results to the GEE-derived results. The advantage of cloud computing would be lost, increasing the computational resources significantly, but it would be informative regarding the quality of GEE preprocessing and the feasibility of Sentinel-1 data. Furthermore, georeferencing techniques could improve the alignment of individual images before taking the backscatter minima and variance. Taking an initial image and mapping all subsequent acquisitions onto that reference could increase the overall quality and diminish the remaining granular texture of composite images. Additionally, implementing the Refined Lee Filter (RLF), designed to preserve linear structures, would reduce speckle noise but spatially smooth the image. Whether necessary detail would be lost needs proper assessment, which could be done in a primitive case study.

Another option would be to use the Sentinel-2 classification as a 'soft' reference. Essentially, channels can be delineated and mapped manually onto the Sentinel-1 data. In hindsight, doing so would have been better as it completely nullifies most issues related to an incorrect reference classification and alleviates some misalignment issues. Note that this would not solve the issue addressed in the Russell study case, where part of the channel remained invisible in Sentinel-1 data.

Machine Learning Strategies

Currently, the GLCM texture features and the backscatter statistics are assumed to cluster in the overall feature space. However, such analysis has not been done throughout this study. Performing cluster analysis for various clustering methods would confirm whether this is indeed the case, and it may reveal additional classes other than the current water and non-water. Additionally, unsupervised learning does not require a reference to the Sentinel-2 classification. Instead, clusters will be based purely on Sentinel-1 data and features. Sentinel-2 could serve as a reference classification for the channels.

Generally, random forest regression (and classification) are not the best for spatial pattern recognition. Machine learning, and deep learning in particular, is a rapidly developing field at the forefront of data analysis. For channel delineation, spatial patterns are crucial and require appropriate identification methods. While the random forest regressor is assisted by the GLCM properties of a 3-by-3 window, larger and more complex structures are not encapsulated by this simplified representation of spatial texture. One option would be to expand the GLCM parameters by considering longer distances (e.g. an additional 5-by-5 kernel) or further discretize the angles; however, alternative methods may prove to be more suitable due to the already prohibitively computationally expensive calculations. In a terrestrial context, convolutional neural networks, among other more advanced techniques, have shown increased performance at image segmentation (Boston et al., 2022; Li et al., 2021; Yoo et al., 2019). Furthermore, detecting cracks in roads and buildings is already widely done using deep learning among other more advanced machine learning methods (Hamishebahar et al., 2022; Hsieh & Tsai, 2020; Zhang et al., 2016). Since this is highly related to channel detection as they resemble 'cracks', transfer learning could be applied. Taking a pre-trained convolutional neural network in the context of civil engineering and adjusting it to the problem of supraglacial channel detection would possibly perform well. Whether the SAR data contains the information necessary to delineate channels would remain a limiting factor, as seen in the Russell study case.

Bibliography

Bell, R. E., Chu, W., Kingslake, J., Das, I., Tedesco, M., Tinto, K. J., Zappa, C. J., Frezzotti, M., Boghosian, A., & Lee, W. S. (2017). Antarctic ice shelf potentially stabilized by export of meltwater in surface river. *Nature*, *544*(7650), 344–348.

Boston, T., Van Dijk, A., Larraondo, P. R., & Thackway, R. (2022). Comparing cnns and random forests for landsat image segmentation trained on a large proxy land cover dataset. *Remote Sensing*, *14*(14), 3396.

Caballero, G. R., Platzeck, G., Pezzola, A., Casella, A., Winschel, C., Silva, S. S., Ludueña, E., Pasqualotto, N., & Delegido, J. (2020). Assessment of multi-date sentinel-1 polarizations and glcm texture features capacity for onion and sunflower classification in an irrigated valley: An object level approach. *Agronomy*, *10*(6), 845.

Copernicus. (2024). Satellite Greenland Ice Sheet Velocity [Accessed: 2024-05-28]. https://www.copernicus.eu/en/access-data/copernicus-services-catalogue/satellite-greenland-ice-sheet-velocity

Corr, D., Leeson, A., McMillan, M., Zhang, C., & Barnes, T. (2022). An inventory of supraglacial lakes and channels across the west antarctic ice sheet. *Earth System Science Data*, *14*(1), 209–228.

Dirscherl, M., Dietz, A. J., Kneisel, C., & Kuenzer, C. (2020). Automated mapping of antarctic supraglacial lakes using a machine learning approach. *Remote Sensing*, *12*(7), 1203.

Dirscherl, M., Dietz, A. J., Kneisel, C., & Kuenzer, C. (2021). A novel method for automated supraglacial lake mapping in antarctica using sentinel-1 sar imagery and deep learning. *Remote Sensing*, *13*(2), 197.

Glen, E., Leeson, A. A., Banwell, A. F., Maddalena, J., Corr, D., Noël, B., & McMillan, M. (2024). A comparison of supraglacial meltwater features throughout contrasting melt seasons: Southwest greenland. *EGUsphere*, *2024*, 1–31.

Halberstadt, A. R. W., Gleason, C. J., Moussavi, M. S., Pope, A., Trusel, L. D., & DeConto, R. M. (2020). Antarctic supraglacial lake identification using landsat-8 image classification. *Remote Sensing*, *12*(8), 1327.

Hamishebahar, Y., Guan, H., So, S., & Jo, J. (2022). A comprehensive review of deep learning-based crack detection approaches. *Applied Sciences*, *12*(3), 1374.

Hillebrand, T. R., Hoffman, M. J., Perego, M., Price, S. F., & Howat, I. M. (2022). The contribution of humboldt glacier, northern greenland, to sea-level rise through 2100 constrained by recent observations of speedup and retreat. *The Cryosphere*, *16*(11), 4679–4700.

Hochreuther, P., Neckel, N., Reimann, N., Humbert, A., & Braun, M. (2021). Fully automated detection of supraglacial lake area for northeast greenland using sentinel-2 time-series. *Remote Sensing*, *13*(2), 205.

Hsieh, Y.-A., & Tsai, Y. J. (2020). Machine learning for crack detection: Review and model performance comparison. *Journal of Computing in Civil Engineering*, *34*(5), 04020038.

IPCC. (2021). *Climate change 2021: The physical science basis* (V. Masson-Delmotte, P. Zhai, A. Pirani, S. Connors, C. Péan, S. Berger, N. Caud, Y. Chen, L. Goldfarb, M. Gomis, M. Huang, K. Leitzell, E. Lonnoy, J. Matthews, T. Maycock, T. Waterfield, O. Yelekçi, R. Yu, & B. Zhou, Eds.). Cambridge University Press. https://www.ipcc.ch/report/ar6/wg1/

Jiang, D., Li, X., Zhang, K., Marinsek, S., Hong, W., & Wu, Y. (2022). Automatic supraglacial lake extraction in greenland using sentinel-1 sar images and attention-based u-net. *Remote Sensing*, *14*(19), 4998.

Li, A., Fan, M., Qin, G., Xu, Y., & Wang, H. (2021). Comparative analysis of machine learning algorithms in automatic identification and extraction of water boundaries. *Applied Sciences*, *11*(21), 10062.

Liang, J., & Liu, D. (2020). A local thresholding approach to flood water delineation using sentinel-1 sar imagery. *ISPRS journal of photogrammetry and remote sensing*, *159*, 53–62.

Lund, J., Forster, R. R., Deeb, E. J., Liston, G. E., Skiles, S. M., & Marshall, H.-P. (2022). Interpreting sentinel-1 sar backscatter signals of snowpack surface melt/freeze, warming, and ripening, through field measurements and physically-based snowmodel. *Remote Sensing*, *14*(16), 4002.

Lutz, K., Bahrami, Z., & Braun, M. (2023). Supraglacial lake evolution over northeast greenland using deep learning methods. *Remote Sensing*, *15*(17), 4360.

Ma, W., Xiao, P., Zhang, X., Song, Y., Ma, T., & Ye, L. (2020). Retrieving snow wetness based on surface and volume scattering simulation. *ISPRS Journal of Photogrammetry and Remote Sensing*, *169*, 17–28.

Miles, K. E., Willis, I. C., Benedek, C. L., Williamson, A. G., & Tedesco, M. (2017). Toward monitoring surface and subsurface lakes on the greenland ice sheet using sentinel-1 sar and landsat-8 oli imagery. *Frontiers in Earth Science*, *5*, 251152.

Mohammadpour, P., Viegas, D. X., & Viegas, C. (2022). Vegetation mapping with random forest using sentinel 2 and glcm texture feature—a case study for lousã region, portugal. *Remote Sensing*, *14*(18), 4585.

Moussavi, M., Pope, A., Halberstadt, A. R. W., Trusel, L. D., Cioffi, L., & Abdalati, W. (2020). Antarctic supraglacial lake detection using landsat 8 and sentinel-2 imagery: Towards continental generation of lake volumes. *Remote Sensing*, *12*(1), 134.

Murashkin, D., Spreen, G., Huntemann, M., & Dierking, W. (2018). Method for detection of leads from sentinel-1 sar images. *Annals of Glaciology*, *59*(76pt2), 124–136.

Obida, C. B., Blackburn, G. A., Whyatt, J. D., & Semple, K. T. (2019). River network delineation from sentinel-1 sar data. *International Journal of Applied Earth Observation and Geoinformation*, *83*, 101910.

Polar Geospatial Center. (2024). ArcticDEM [Accessed: 2024-05-28]. https://www.pgc.umn.edu/data/arcticdem/

Rawlins, L. D., Rippin, D. M., Sole, A. J., Livingstone, S. J., & Yang, K. (2023). Seasonal evolution of the supraglacial drainage network at humboldt glacier, north greenland, between 2016 and 2020. *The Cryosphere Discussions*, *2023*, 1–32.

Rignot, E., An, L., Chauche, N., Morlighem, M., Jeong, S., Wood, M., Mouginot, J., Willis, J. K., Klaucke, I., Weinrebe, W., et al. (2021). Retreat of humboldt gletscher, north greenland, driven by undercutting from a warmer ocean. *Geophysical research letters*, *48*(6), e2020GL091342.

Rignot, E., Casassa, G., Gogineni, P., Krabill, W., Rivera, A., & Thomas, R. (2004). Accelerated ice discharge from the antarctic peninsula following the collapse of larsen b ice shelf. *Geophysical research letters*, *31*(18).

Rignot, E., Gogineni, S., Joughin, I., & Krabill, W. (2001). Contribution to the glaciology of northern greenland from satellite radar interferometry. *Journal of Geophysical Research: Atmospheres*, *106*(D24), 34007–34019.

Sasgen, I., Wouters, B., Gardner, A. S., King, M. D., Tedesco, M., Landerer, F. W., Dahle, C., Save, H., & Fettweis, X. (2020). Return to rapid ice loss in greenland and record loss in 2019 detected by the grace-fo satellites. *Communications Earth & Environment*, *1*(1), 1–8.

Scambos, T. A., Hulbe, C., Fahnestock, M., & Bohlander, J. (2000). The link between climate warming and break-up of ice shelves in the antarctic peninsula. *Journal of Glaciology*, *46*(154), 516–530.

Sundal, A., Shepherd, A., Nienow, P., Hanna, E., Palmer, S., & Huybrechts, P. (2009). Evolution of supra-glacial lakes across the greenland ice sheet. *Remote Sensing of Environment*, *113*(10), 2164–2171.

Tan, J., Tang, Y., Liu, B., Zhao, G., Mu, Y., Sun, M., & Wang, B. (2023). A self-adaptive thresholding approach for automatic water extraction using sentinel-1 sar imagery based on otsu algorithm and distance block. *Remote Sensing*, *15*(10), 2690.

Uddin, K., Matin, M. A., & Meyer, F. J. (2019). Operational flood mapping using multi-temporal sentinel-1 sar images: A case study from bangladesh. *Remote Sensing*, *11*(13), 1581.

Williamson, A. G., Banwell, A. F., Willis, I. C., & Arnold, N. S. (2018). Dual-satellite (sentinel-2 and landsat 8) remote sensing of supraglacial lakes in greenland. *The Cryosphere*, *12*(9), 3045–3065.

Yang, K., Karlstrom, L., Smith, L. C., & Li, M. (2016). Automated high-resolution satellite image registration using supraglacial rivers on the greenland ice sheet. *IEEE Journal of Selected Topics in Applied Earth Observations and Remote Sensing*, *10*(3), 845–856.

Yang, K., Li, M., Liu, Y., Cheng, L., Huang, Q., & Chen, Y. (2015). River detection in remotely sensed imagery using gabor filtering and path opening. *Remote Sensing*, *7*(7), 8779–8802.

Yang, K., & Smith, L. C. (2012). Supraglacial streams on the greenland ice sheet delineated from combined spectral–shape information in high-resolution satellite imagery. *IEEE Geoscience and Remote Sensing Letters*, *10*(4), 801–805.

Yang, K., Smith, L. C., Sole, A., Livingstone, S. J., Cheng, X., Chen, Z., & Li, M. (2019). Supraglacial rivers on the northwest greenland ice sheet, devon ice cap, and barnes ice cap mapped using sentinel-2 imagery. *International Journal of Applied Earth Observation and Geoinformation*, *78*, 1–13.

Yoo, C., Han, D., Im, J., & Bechtel, B. (2019). Comparison between convolutional neural networks and random forest for local climate zone classification in mega urban areas using landsat images. *ISPRS Journal of Photogrammetry and Remote Sensing*, *157*, 155–170.

Zhang, L., Yang, F., Zhang, Y. D., & Zhu, Y. J. (2016). Road crack detection using deep convolutional neural network. *2016 IEEE international conference on image processing (ICIP)*, 3708–3712.

Zheng, L., Li, L., Chen, Z., He, Y., Mo, L., Chen, D., Hu, Q., Wang, L., Liang, Q., & Cheng, X. (2023). Multi-sensor imaging of winter buried lakes in the greenland ice sheet. *Remote Sensing of Environment*, *295*, 113688.

Lastly, ChatGPT has been utilized as a tool to generate, adjust and optimize Python code. It has been used in combination with Grammarly to assist in writing and proposing prompts for the introduction, which have been rewritten manually.